TECHNISCHE UNIVERSITÄT WIEN

# Time-resolved GATE simulations of the $\beta^+$-activity after proton irradiation

Diplomarbeit

zur Erlangung des akademischen Grades

**Diplom-Ingenieurin**

im Rahmen des Studiums

**Biomedical Engineering**

eingereicht von

**Elka Xharo**
Matrikelnummer 0826553

Ausgeführt am
Atominstitut
der Technischen Universität Wien

Betreuer:
Univ.Prof. civ.ing. tekn.lic. tekn.dr. Lembit Sihver
Co-Betreuerin:
Dipl.-Math. Dr.rer.medic. Heide Rohling

Wien, April 2017

# Statutory Declaration

I declare that I have authored this thesis independently, that I have not used other than the declared sources/resources, and that I have explicitly marked all material which has been quoted either literally or by content from the used sources.

Vienna, _____ _____

Date Signature

# Acknowledgements

# Kurzfassung

Protonentherapie ermöglicht eine besonders präzise und schonende Behandlung von KrebspatientInnen. Sie ist jedoch empfindlicher auf Ungenauigkeiten als die konventionelle Strahlentherapie mit Photonen, weshalb eine nicht-invasive in-vivo Dosisverifikation wünschenswert ist. Die einzige klinisch angewandte Methode zur 3D Dosisverifikation ist *Positronen-Emissions-Tomographie (PET)*. Die Bestrahlungsdosis kann jedoch nicht direkt aus den PET-Messdaten ermittelt werden. Die PET-Messdaten müssen mit vorhergesagten PET-Daten aus Computersimulationen verglichen werden. Die Software GATE stellt ein Werkzeug für die Simulation der durch Protonenbestrahlung erzeugten $\beta^+$-Aktivität dar.
Die vorliegende Arbeit befasst sich mit GATE-Simulationen, die an den Ablauf des PET-Monitorings am MedAustron-Zentrum angepasst sind. Es handelt sich hierbei um *offline PET*, d.h. der PET Scanner ist nicht direkt im Behandlungsraum platziert. Es wird untersucht, welche Nuklid in die Simulationen miteinbezogen werden sollten und welche Auswirkungen biologischer Washout (Auswaschung) und die zeitliche Komponente haben. Außerdem wurde eine neue Implementierung in GATE, der *CrossSectionProductionActor (CS-Actor)*, evaluiert.
Zur Untersuchung dieser Themenbereiche wurde die Bestrahlung eines PMMA-Targets und eines auf einem CT-Scan (Computertomographie) basierenden modellierten menschlichen Schädels simuliert. Außerdem wurde die Anwendung eines vollständigen Bestrahlungsplans simuliert.
Die Auswertung dieser Simulationen deutet darauf hin, dass für die Reichweitenverifikation die Simulation von $^{11}$C ausreichend ist. Wenn

höhere Genauigkeit erforderlich ist, empfiehlt sich jedoch die Einbeziehung von $^{13}$N. Weiters wurde gezeigt, dass die Berücksichtigung von Bestrahlungszeit und biologischem Washout ausschlaggebend ist. Die Bestrahlungszeit, während der Radionuklid gleichzeitig entstehen und zerfallen, ist noch nicht in die GATE-Software eingebaut. Eine Erweiterung von GATE und weitere Anpassungen des Washout-Modells sind nötig.
Es hat sich herausgestellt, dass der CS-Actor bessere Übereinstimmungen zum verwendeten experimentellen Datensatz und schnellere Ergebnisse als der etablierte Actor, der vollständig auf der stochastischen Monte Carlo Methode basiert, erzielt. Abgesehen von kleineren Problemen könnte der CS-Actor eine geeignete Alternative für die klinische Praxis darstellen. Im Moment ist er nur für die Simulation der Nuklide $^{11}$C und $^{15}$O verfügbar, weshalb eine Erweiterung des CS-Actors wünschenswert ist.

# Abstract

Proton radiotherapy can assure a more precise treatment of cancer patients, but is more sensitive to uncertainties than conventional radiotherapy using photons. Therefore, non-invasive in-vivo dose verification is desired. The only clinically applied method for 3D dose verification in proton therapy is *positron emission tomography (PET) monitoring*. Because of the different underlying physical processes, the dose cannot be deduced directly from the measured PET data. The measured PET data needs to be compared to predicted PET data, generated by simulations. The GATE software provides a useful tool for the simulation of $\beta^+$-activity induced by proton irradiation.
The present work focuses on GATE simulations suitable for the workflow at the MedAustron facility. The implemented modality at MedAustron is an *offline PET*, i.e. the PET scanner is not located in the treatment room. This thesis investigates which nuclides need to be included in the simulation, and what impact the time structure and biological washout have. Finally, a new simulation approach in GATE, the *CrossSectionProductionActor (CS-Actor)*, was evaluated.
To investigate these topics, the $\beta^+$-activity following the irradiation of a PMMA target and a patient's head were simulated. Also, a full radiotherapy plan was simulated using a modelled human head, based on a CT (computed tomography) scan, as the target.
The evaluation of the simulations suggests that for range verification, the simulation of $^{11}$C might be sufficient. However, if a higher accuracy is needed, the inclusion of $^{13}$N is recommended. The importance of including the irradiation time and biological washout was shown as well. The irradiation time, during which production and decay of

nuclides take place simultaneously, is the only aspect not yet included in GATE. An extension of GATE and a further examination of the implemented biological washout model is needed.
It was found that the CS-Actor is faster and more accurate than the established Actor that fully relies on a Monte Carlo method, a stochastic numerical technique. Apart from some smaller problems, the CS-Actor could be an applicable alternative. At the moment, the CS-Actor is only available for the simulation of $^{11}$C and $^{15}$O. Therefore, an extension of the Actor to simulate $^{13}$N is desirable.

# List of abbreviations

| | |
|---|---|
| **CS-Actor** | CrossSectionProductionActor |
| **CT** | Computed tomography |
| **DNA** | Deoxyribonucleic acid |
| **HU** | Hounsfield unit |
| **JAM** | Jet AA Microscopic Transport Model |
| **LHC** | Large Hadron Collider |
| **MC method** | Monte Carlo method |
| **MC simulation** | Monte Carlo simulation |
| **MRI** | Magnetic resonance imaging |
| **PGI** | Prompt gamma imaging |
| **PET** | Positron emission tomography |
| **PMMA** | Polymethyl methacrylate |
| **PS-Actor** | ProductionAndStoppingActor |

| | |
|---|---|
| **PT-PET** | Particle therapy positron emission tomography |
| **RT** | Radiation therapy |
| **SOBP** | Spread-out Bragg peak |
| **QMD** | Quantum Molecular Dynamics |

# Contents

~

# 1 Introduction

Cancer is among the most deadly diseases in the industrialised world. Despite high investments in cancer research and significant improvements in therapy, 26% of the deaths in the EU are still caused by cancer [1].

In about half of the cases, radiation therapy is one of the applied treatment modalities [2]. Scientific progress in medicine is decreasing the mortality rate of cancer patients constantly, but especially for complicated locations surrounded by delicate tissue, treatment with conventional photon radiation therapy, as well as surgery, is either risky or not applicable.

By using protons instead of photons, a more precise form of radiation therapy was developed. Due to its physical properties, proton therapy can assure less damage to nearby healthy tissue. Therefore, it permits the irradiation of patients with tumours in the cranium or near the spinal cord. Proton therapy is also highly recommended in paediatric treatments, because of its lower dose in surrounding tissue and fewer side effects.

The field of proton therapy is still growing, about 64 facilities offer this type of therapy. One of them, the MedAustron facility, is situated in Wiener Neustadt, Austria. MedAustron already performs proton therapy and will also offer carbon ion therapy.
Adapted to the operational modality of MedAustron, simulations for dose verification after proton therapy were performed for this thesis.

# 1 Introduction

Proton therapy is highly sensitive to inaccuracies through movement or other factors. To assure a precise application, dose verification is desirable. The only clinically applied method for 3D dose verification is using PET monitoring to measure the $\beta^+$-activity produced by the beam. To verify the dose deposition of the beam, this measured PET data needs to be compared to predicted PET data that is generated by simulations. The software GATE, used in this thesis, is one possible tool for these simulations [3].

The topic of this thesis was the question: which $\beta^+$-emitters need to be considered in the simulations for offline PET, the operational modality at MedAustron. Therefore, the activity of the $\beta^+$-emitters was modelled including the time structure of the PET monitoring workflow and biological washout.
Finally, the results of two different simulation approaches in GATE were evaluated.

# 2 State of the art

The chapter will provide an overview of the relevant theoretical background for this thesis. The basic concepts of proton therapy, positron emission tomography monitoring (PET monitoring) and particle transport simulations will be presented.

## 2.1 Proton therapy

Proton therapy is a special kind of radiation therapy (radiotherapy or RT), using protons instead of the conventional radiotherapy of photon or electron beams. It is categorised as one form of hadron therapy. Hadron therapy includes radiotherapy with particles that are made of quarks, mostly proton and carbon ion therapy [4].

In cancer treatment, radiotherapy is one of the most common therapy modalities. The aim of radiotherapy is to destroy tumourous cells (cells with abnormal growth) through ionizing radiation.
The radiation may be delivered from inside the body, via radioactive implants near or inside the tumour, called Brachytherapy, or by drinking or injecting a liquid nuclide. Radiation may as well be applied from outside the body, known as external beam radiotherapy (tele therapy). This is the most common form of radiotherapy [5].

The high-energy radiation damages the DNA of cells, and can make it impossible for them to divide [6]. Cancerous cells show a higher

sensibility to ionizing radiation than healthy cells, because their ability to repair this biological damage is lower [7]. Taking advantage of this behaviour is the basic concept of radiotherapy. However, the damage of healthy cells still cannot be avoided completely. Improving the protection of healthy cells is the main motivation for the development of proton therapy.

The conventional radiation method has been using photon beams for more than one hundred years [4].
It was in 1946, Robert Wilson, a physicist from the United States, first proposed the use of protons in radiotherapy [8]. He based his suggestion on the advantageous physical properties of the dose deposition of protons.

Figure 2.1 compares the dose deposition of photons, protons and carbon ions. This varying behaviour was first discovered by William Henry Bragg in 1905 [9]. Therefore, the curve is known as *Bragg curve*. Protons, and heavy ions, deposit a large part of their energy at the end of their range, while photons penetrate the body with an approximately uniform dose deposition. The dose deposition works through energy transfer from the projectile to the tumour cells. The projectiles, in our case protons, interact with the shell electrons of tissue molecules, and induce excitation and ionization of atoms and molecules in the tissue. By using the *Bethe-Bloch* formula, the energy loss of a charged particle along its path can be described [2].
In the beginning of their penetration track, protons depose less dose. They slow down in the tissue, until they are finally stopped. While slowing down, more interactions take place. The dose disposition reaches a high peak, the *Bragg peak*, before it falls down to zero, within millimetres [7].
This allows for a precise dose deposition and better protection of the healthy tissue, located in beam direction behind the Bragg peak, than with photon beams.

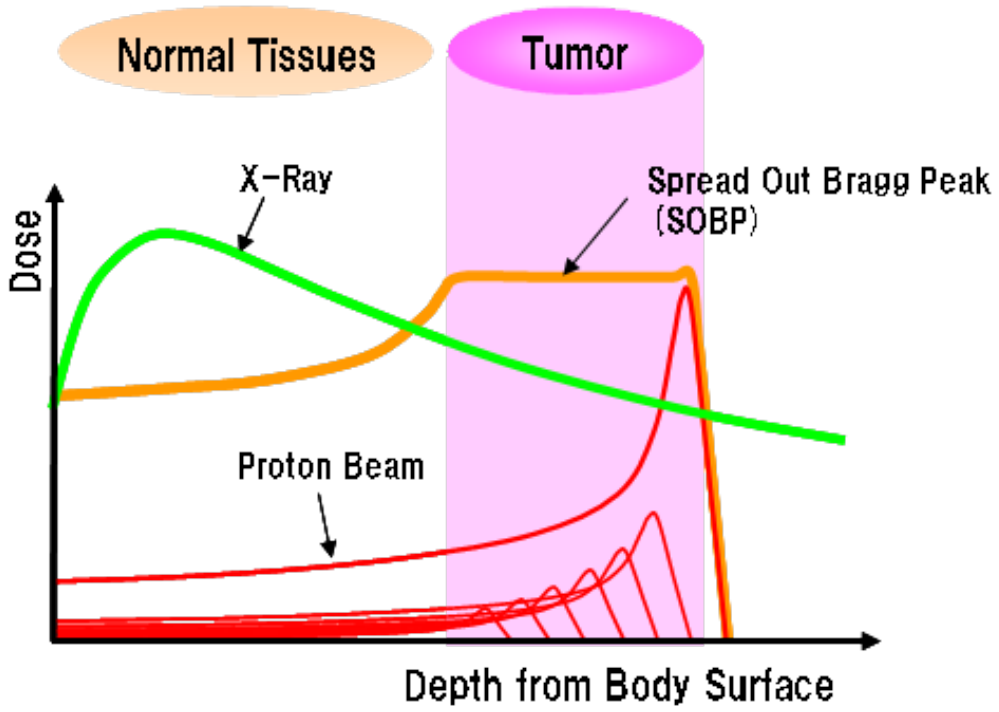


Figure 2.1: Comparison of bragg curves of photons, protons and carbon ions [10]

To uniformly cover a broader area of the tumour, various proton beams with different energies, and therefore different ranges, can be combined, resulting in a *spread-out Bragg peak* (SOBP). When using a SOBP, the dose in the depth before the Bragg peak can be relatively high. However, the significant advantage of proton beams is the distal fall off after the Bragg peak. Organs at risk which are located directly behind the Bragg peak, can be protected from irradiation. Though, this narrow Bragg peak can be the source for uncertainties in proton irradiation, as will be discussed later [5].

The very first proton therapy patient was treated in 1954 at Lawrence Berkeley Laboratory [11]. The number of patients being treated with

protons rises every year, but it is still just a small fraction of all radiotherapy patients. Most radiotherapies are still performed with photons, because proton therapy involves significantly higher costs than conventional radiotherapy [11]. Besides, it was found that only 15% of the patients that are treated with conventional radiation would profit significantly from hadron therapy [4].

### MedAustron

Worldwide, there are currently 64 operating facilities that offer proton therapy, and only six facilities with proton as well as carbon ion therapy [12]. One of these six facilities, MedAustron, is situated in Wiener Neustadt, Austria. It already offers proton therapy; carbon ion therapy will be available after 2018.

The construction started in 2011, and at the end of 2016 the first patient irradiation was performed. About 1,000 patients will be treated per year in the facility [13].

MedAustron has been equipped with a synchrotron, in order to provide the acceleration of both proton and carbon ions in one machine [13]. In contrast, cyclotrons cannot be used for carbon ion beams with high energies as required for radiation therapy. Synchrotrons allow the production and fast variation of energies. However, synchrotrons are larger in size and more cost-intensive than cyclotrons [11].

In addition to clinical treatments, the accelerator is also used for clinical and non-clinical research. The focus is on *Radiobiology*, *Medical Radiation Physics* and *Radiation Physics* [14].

Figure 2.2 is a schematic plan of the MedAustron facility. It shows the

circular accelerator and the four different irradiation rooms.

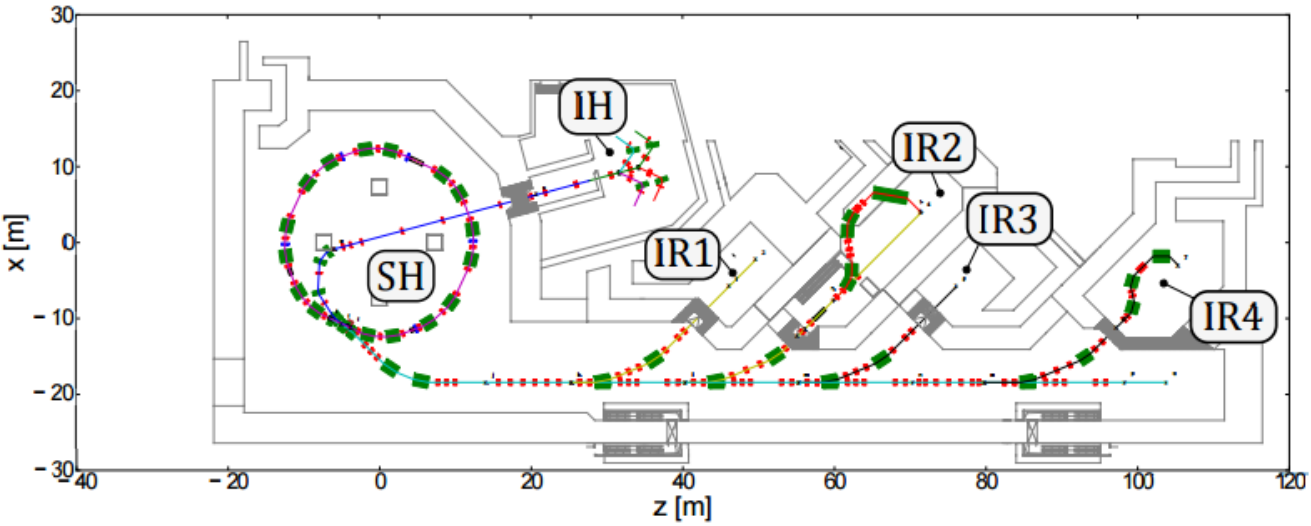


Figure 2.2: Overview of the accelerator facilities of MedAustron with synchrotron hall (SH), injection hall (IH) and four irradiation rooms (IR1-IR4) [13]

The first three rooms will offer both proton and carbon ion irradiation, while the fourth will be equipped with a proton gantry. The first room is currently used for research.
The synchrotron can accelerate protons up to 800 MeV. However, for medical treatment, only protons in the energy range 62-257 MeV will be used. In comparison, photon beam therapy operates with only 20 kV - 20 MV. The most common acceleration voltage is 6 and 15 MV [15].

Mainly patients with tumours in highly sensitive locations, will be treated at MedAustron. Because of the aforementioned Bragg curve, hadron therapy causes less damage to the nearby healthy tissue. Therefore, it is especially recommended for tumours that are near radiation

sensitive tissue, like the eye, brain or spinal cord. The lower side effects are also a reason why it is often used for paediatric tumours [14]. In general, proton therapy is used for cases where neither surgery nor conventional photon therapy is applicable.

Figure 2.3 shows the treatment equipment in one of the irradiation rooms at MedAustron. The patient is wearing a custom-made mask that assures the exact positioning for each treatment.
Surrounding the patient, the so-called *imaging ring* is situated. It is a CT ring, installed directly on the patient table, that checks the accurate positioning before every treatment [14].

Figure 2.3: Proton therapy treatment at MedAustron [14]

Immobilization devices help to reduce inaccuracies through movement or incorrect positioning. This is crucial, especially for proton therapy. Because of its narrow Bragg peak, proton beam therapy is more sensitive to inaccuracies than radiotherapy using photons.
On the one hand, the narrow Bragg peak is an essential benefit, but on the other hand, the smallest inaccuracies can lead to a dislocation of the Bragg peak, resulting in deposition of high doses in healthy tissue and/or almost no dose in the tumour. Therefore, monitoring and non-invasive in-vivo verification of dose deposition is desired.

## 2.2 In-vivo dose verification

Dose uncertainties in hadron therapy can have various reasons. During treatment, they can result from positioning errors, but also from breathing, organ motion or interfractional size changes of the tumour. Another source of uncertainty arises from CT conversion. To be able to use the CT scans for the irradiation planning, the scan must be converted to tissue type and density maps. This conversion, along with basic stochastic errors in the CT, caused by resolution, artefacts or noise, can corrupt the accuracy of the planning [16].

There are several techniques for non-invasive in vivo verification, but most of them are not yet clinically applied.
Prompt gamma imaging (PGI) measures $\gamma$-rays produced by inelastic interactions of the incident proton with the nuclei of the target [2]. However, at the moment there are no practical detectors for clinical PGI available [16].
Magnetic resonance imaging (MRI) can be used to visualise the physiological changes caused by proton therapy. However, this would require a waiting time of several weeks until the physiological changes develop [16].
The only clinically applied method for 3D in-vivo dose monitoring is

to use PET monitoring. This method is also known as particle therapy positron emission tomography (PT-PET). It is the only method that has been applied successfully in clinical routines for 3D in-vivo dose verification for hadron therapy [2]. In PT-PET, the annihilation photons of the $\beta^+$-activity of the nuclides produced by the proton beam is measured to verify the dose application.
To understand the functionality of PT-PET, at first the basic concept of PET will be described.

### 2.2.1 Basic concept of PET in nuclear medicine

PET is a functional imaging technique for the visualisation of $\beta^+$-emitters. It can visualise metabolic processes in the body.
PET is mostly used for diagnosis. A radioactively labelled compound, called radiotracer, is injected in the patient's body. The most common tracer is fludeoxyglucose. Tumourous cells have a different metabolism than healthy cells; they show a higher energy uptake. Therefore, the tracer will mainly move to the tumourous tissue. The annihilation photons can then be detected with the PET scanner [17].
During $\beta^+$-decay, the radioactive nucleus emits a positron $e^+$ and an electron neutrino $v_e$:

$$ {}^{A}_{Z}X \rightarrow {}^{A}_{Z-1}Y + e^+ + v_e \tag{2.1} $$

The emitted positron annihilates with one electron in the body and produces a pair of annihilation photons.

$$ e^+ + e^- \rightarrow 2\,\gamma \tag{2.2} $$

Annihilation photons move in opposite directions to each other and can thereupon leave the body [18]. These photons can now be detected

through the circularly arranged detectors of the PET scanner, as depicted in figure 2.4. On the basis of these two coinciding signals, it is possible to localize the source of the annihilation event and thereupon generate an image reconstruction [17].

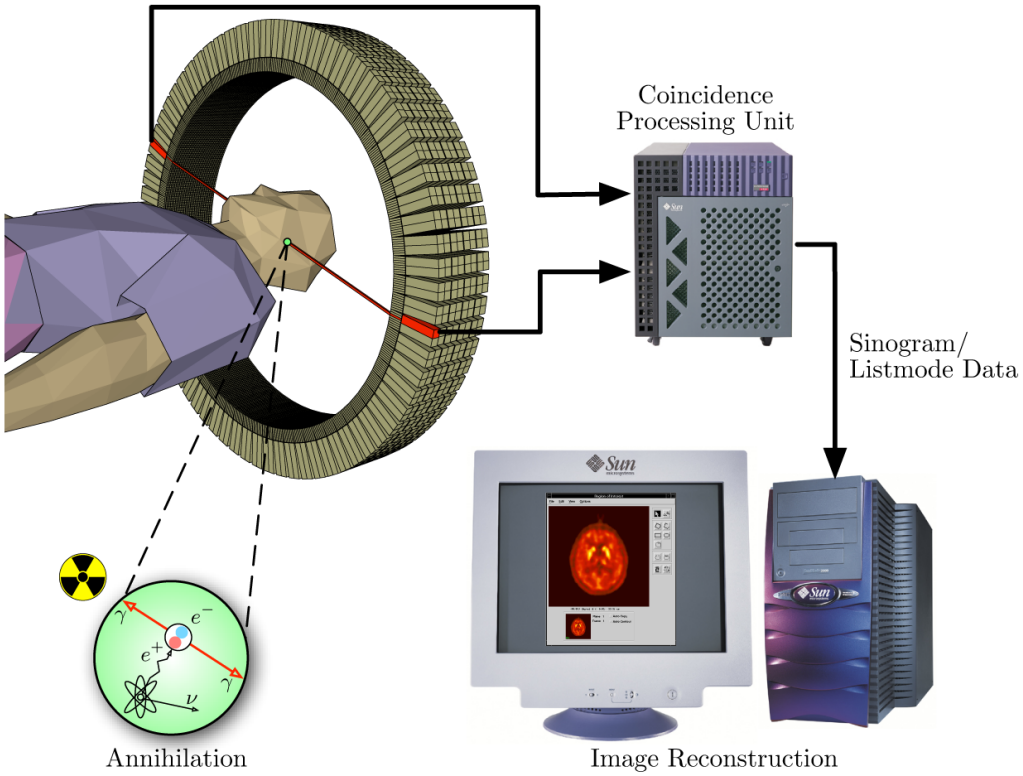


Figure 2.4: Functionality of PET acquisition, [19]

To achieve a 3D image, modern PET is often combined with CT scan, resulting in PET-CT scanners. Combining the topological information of CT, and the functional information of the PET can assure an accurate spatial reconstruction.

### 2.2.2 PT-PET

In 1969, Maccabee *et al* put forward the idea of using PET for dose verification in hadron therapy [16]. In 1984, the first application took place at Lawrence Berkeley Laboratory [2].

The idea of PET monitoring is to measure the $\beta^+$-activity of the nuclides produced by interactions between the beam particles and the atoms of the tissue. Dose verification in proton therapy is usually confined to range verification, because the location of the highest energy deposition is highly dependent on the proton range. Range verification is focused on comparing the distal fall off and the the fall offs in cavities of the distributions of annihilation points of measured and predicted data. It is done either point-wise or by shifting it [16].

There are different approaches concerning the spatial and temporal implementation of PET monitoring, namely in-beam PET, in-room PET and offline PET [20].
With in-beam PET, the monitoring takes places quasi-simultaneously to the therapy, by measuring in the pauses of the pulsed irradiation. The PET scanner is integrated in the treatment room.
The in-room PET is a separate device, but located in the same room. Therefore, the time to transport the patient to the PET scanner after the irradiation is relatively short, and done by a robot. No patient repositioning is required.
In offline PET, the PET scanner is located in a different room. A transport time of 5-10 minutes must be taken into account. An offline PET, namely a Philips Gemini TF Big Bore PET/CT, is installed at MedAustron, and therefore the considered modality for this thesis.

The major challenge of PET monitoring is the low activity in the PET measurements. Besides, the dose cannot be deduced directly from this PET measurements, hence the activity of the secondary

particles. The reason is the different underlying physical processes involved. The dose deposition involves interactions with the electrons of the tissue, meanwhile $\beta^+$-activity is produced by nucleus-nucleus collisions [2].

To verify the dose deposition, the measured PET data needs to be compared to predicted PET data, generated from computer simulations. Therefore, exact simulations of the $\beta^+$-activity are needed. Along with the already mentioned factors of uncertainties in radiotherapy (motion, organ movement, tumour size changes), biological washout effect and inaccuracies in the simulation are one of the main sources of uncertainties in PET monitoring [16]. Especially for offline PET, the correction of biological washout is crucial [16]. Biological washout arise mainly due to blood flow. In tissue with high perfusion, this leads to much lower yields.
The uncertainties in the simulations are mostly caused by uncertainties in the used cross-section data.

For the offline PET application at MedAustron it should be clarified which nuclides should be included in the simulation, for assuring an accurate solution, and at the same time, guaranteeing an acceptable execution time.
The choice of the nuclides depends significantly on the abundance and half-life of the nuclides. However, the included nuclides vary depending on the operational modality. In offline PET, short-lived nuclides that are relevant for in-beam PET might have already been decayed. Besides, taking into account the biological washout and time-dependency is crucial in offline PET simulations [21].

The following nuclides were discussed in previous studies about in-beam or in-room PET in proton therapy:
Rohling *et al* 2013 include $^{11}$C and $^{15}$O and $^{13}$N in their simulations during proton irradiation [22].
Parodi *et al* 2002 focus on $^{11}$C, $^{15}$O and $^{10}$C, and emphasize the signifi-

cance of short-lived $^{15}$O for in-beam PET [23].

The following publications studied offline PET in proton therapy:
Zhu and El Fakhri 2012 list $^{11}$C, $^{15}$O and $^{13}$N as the most important radionuclide species in soft tissue, and mention that offline PET mostly measures $^{11}$C [16].
Bauer *et al* 2013 and the Heidelberg Ion-Beam Therapy Center (HIT) include $^{11}$C, $^{15}$O, $^{13}$N, $^{30}$P and $^{38}$K in their study [24].
Parodi *et al* 2007 include $^{11}$C,$^{15}$O, $^{13}$N, $^{38}$K and $^{30}$P in their publication [25].

Seravalli *et al* 2012 investigate the production rates of $^{15}$O and $^{11}$C in their simulations for proton therapy in general [26].
Pshenichnov *et al* 2006 calculate the production rates for $^{11}$C,$^{15}$O and $^{10}$C for proton and $^{12}$C therapy, and declare $^{11}$C as the most suitable nuclide for PET monitoring [27].

For PET monitoring in carbon ion therapy the simulation has to be slightly different, because carbon nuclides can also appear as projectile fragments. The following studies discuss carbon ion therapy:
Rohling *et al* 2013 include $^{11}$C, $^{15}$O, $^{10}$C and $^{13}$N in their simulations during $^{12}$C irradiation [22].
Jan *et al* 2013 analyse the activity of $^{11}$C and $^{15}$O, and conclude that the contribution of $^{15}$O to the signal fall off is negligible. The study was performed with a carbon ion beam and in-room PET [28].
Bauer *et al* 2013 assert that for offline PET in $^{12}$C irradiation the signal is dominated by the activity of $^{11}$C, while for in-beam PET $^{15}$O dominates [29].

### 2.2.3 Relevant nuclear reactions

To understand the production in terms of location and abundance of the $\beta^+$-emitters, it is helpful to know from which nuclear reactions they derive. Table 2.1 lists the $\beta^+$-emitters that were considered for this thesis, their half-lifes and their nuclear reactions.

Bony structure contains calcium and phosphor. Therefore, $^{30}$P and $^{39}$Ca, which also derive from phosphor and calcium, are expected to be found mainly in bones. $^{15}$O, $^{13}$N and the carbon isotopes derive from $^{16}$O that can be found in soft tissue.

Table 2.1: Nuclear reactions which produce the considered $\beta^+$-emitters [16, 24]

| Nuclide | Half-life [min] | Reaction |
|---|---|---|
| $^{15}O$ | 2.032 | $^{16}O(p,pn)^{15}O$ |
| $^{11}C$ | 20.383 | $^{12}C(p,pn)^{11}C$, $^{16}O(p,3p3n)^{11}C$, $^{14}N(p,2p2n)^{11}C$ |
| $^{13}N$ | 9.967 | $^{16}O(p,2p2n)^{13}N$, $^{14}N(p,pn)^{13}N$ |
| $^{10}C$ | 0.317 | $^{12}C(p,p2n)^{10}C$, $^{16}O(p,3p4n)^{10}C$ |
| $^{30}P$ | 2.500 | $^{31}P(p,pn)^{30}P$ |
| $^{38}K$ | 7.633 | $^{40}Ca(p,2p2n)^{38}K$ |
| $^{39}Ca$ | 0.014 | $^{40}Ca(p,pn)^{39}Ca$ |
| $^{34}Cl$ | 0.025 | $^{34}S(p,n)^{34}Cl$ |
| $^{9}C$ | 0.02 | $^{12}C(p,p3n)^{9}C$, $^{16}O(p,3p5n)^{9}C$ |

### 2.2.4 Washout model

As mentioned before, the incorporation of the washout effect is crucial for precise simulations, especially for offline PET.
The washout model that is usually used for PET monitoring, is the Mizuno model. It was developed by Mizuno based on experiments with a rabbit and carbon beams [30].

It is defined by a differential equation with three components which represent fast, intermediate and slow washout with tissue-dependent parameters.

$$c(t) = M_f e^{-\lambda_f t} + M_i e^{-\lambda_i t} + M_s e^{-\lambda_s t} \tag{2.3}$$

| | |
|---|---|
| $M_f$ | fast component |
| $M_i$ | intermediate component |
| $M_s$ | slow component |
| $\lambda_{f,i,s}$ | decay constant of fast/intermediate/slow components |
| $t$ | time |
| with | $M_f + M_i + M_s = 1$ |

There are some uncertainties about this washout model. As it was derived from healthy animal tissue, it might overestimate the washout in tumour tissue [29]. Also, it does not apply different washout rates for different radionuclide species, so the same parameters are used for $^{11}$C and $^{15}$O. Finally, there could be a possible inaccuracy for proton irradiation, since the Mizuno model was developed in experiments using a carbon beam [16]. However, there are no better alternatives available. Modelling of washout is still a work in progress.

## 2.3 Simulations for particle transport

The simulation of the predicted PET data is a crucial part of PET monitoring. Only exact simulations can guarantee the best possible monitoring.
Most of the PT-PET simulations are based on the relatively slow (in comparison to deterministic approaches), but sophisticated, Monte Carlo method (MC method). However, there are also other approaches (see section 2.3.2).

### 2.3.1 Monte Carlo simulations

The MC method is a numerical technique which uses the laws of statistics to generate solutions. It has been used for several decades in different fields of science, including particle transport [31]. In the simulation software GATE, most of the simulations are based on MC methods [3].

The principles of MC methods were developed in the 30's, and implemented in the ENIAC (Electronic Numerical Integrator and Computer) [32]. The approach of the MC method is to solve complex problems, where a deterministic solution is either impossible or too time consuming, by relying on the sampling of random numbers [33]. A stochastic model is set up, and the individual values are randomly taken from probability distributions. An accurate solution can be achieved by using a sufficiently large number of random values [6]. The selection of the quantity of random values involves a trade-off with the execution time. The larger the number of random values, the more accurate is the solution, but also the longer is the execution time.

Monte Carlo simulations (MC simulations) are still considered the most accurate approach to predict PET activity distribution [16]. However, there are two main sources of uncertainty. MC simulations substantially rely on the accuracy of the cross-section data that is used for the models. It was discovered that there are significant discrepancies between published cross-section data sets. The other source is the aforementioned CT conversion [16].

### 2.3.2 Particle transport simulation codes

For the calculation of predicted activity distribution, the commonly utilized particle transportations packages are PHITS, FLUKA and

GEANT4 [16].

PHITS (Particle and Heavy-Ion Transport code System) is a general purpose MC particle transport code that has been successfully applied in different fields of research [34]. However, it has been shown that PHITS underestimates the production yield when applied to proton irradiation of water and PMMA targets [22, 26].
FLUKA is another general purpose MC simulation code. It is written in FORTRAN and is the result of a cooperation between many European research institutes [35]. FLUKA is widely used for simulations in activation, dosimetry and particle therapy [26].

GEANT4 is an open-source code originally for Large Hadron Collider (LHC) experiments, but later used in many fields of physics. GEANT4 is written in C++ [36]. GEANT4 has been validated various times and has shown to produce accurate results in proton irradiation [22]. The simulation software GATE that was used for this thesis is based on GEANT4 (see chapter 3.1).

In these particle simulation codes several nuclear reaction models are implemented. In PHITS, the Jet AA Microscopic Transport Model (JAM), the quantum molecular dynamics (QMD) and the Bertini model are available [22].

Besides codes based on MC methods, there is another approach for particle transportation, called HIBRAC. HIBRAC is an one-dimensional deterministic code developed in the 90's by Sihver et al [37]. It was written in FORTRAN and shows promising results [2]. The advantage of HIBRAC is the fact that it is faster than three-dimensional MC simulations. However, HIBRAC's one-dimensional calculations might not be sufficient for a clinical application.
It was developed for treatment planning in ion therapy, but it will be possible to use it in different fields. It has already been used in radiobiology experiments [38].

# 3 Methodology

In this chapter, details about the performed simulations will be given. A short introduction to the simulation software GATE will be covered, followed by technical details and descriptions of the methods and simulations used.

## 3.1 GATE

GATE is an open-source software which is built on top of the multi-purpose simulation toolkit GEANT4 [39]. It was developed by the international OpenGATE collaboration, and provides simulations for medical imaging and radiotherapy. GATE can be used for simulations with PET, SPECT, Optical imaging (Bioluminescence and Fluorescence) and radiotherapy experiments. [40].
It was decided by the research group to apply GATE for the simulation required for PET monitoring at MedAustron due to its user-friendliness and already implemented useful features in this context, i.e. washout and the possible modelling of the PET scanner. Therefore, GATE has also been used for this thesis.
In 2001, during a workshop in Paris, several research groups had the idea to create a new software for MC simulations in nuclear medicine, to improve existing codes. One year later, the first version of GATE was presented, and the OpenGATE collaboration was founded. Researchers from Europe, North America and Asia took part in the collaboration [3].

Since then, the collaboration has grown, and is constantly working on free and open-source releases of the GATE software. They also provide a helpful, but in some parts, still incomplete, users guide [41] and a relatively active mailing list, as a support for GATE users. The source code can be entered and modified through a Git repository.

For this thesis the version 7.2 was used, as it was already installed on the used server. GATE is coded in C++, but one of the requirements of the developing group was that it should be usable without any knowledge of C++. The configuration of the simulations in GATE works through macro scripts.

### 3.1.1 How to use GATE

Below is an exemplary extract of a GATE macro:

```
# World
/gate/world/setMaterial Air
/gate/world/geometry/setXLength 4.0 m
/gate/world/geometry/setYLength 4.0 m
/gate/world/geometry/setZLength 4.0 m

# Box
/gate/world/daughters/name phanbox
/gate/world/daughters/insert box
/gate/phanbox/setMaterial Plastic
/gate/phanbox/geometry/setXLength 10.0 cm
/gate/phanbox/geometry/setYLength 10.0 cm
/gate/phanbox/geometry/setZLength 40.0 cm
/gate/phanbox/placement/setTranslation 0 0 0 cm
```

First a *world* needs to be defined, i.e. a surrounding environment in which the target will be placed. In this case, it is made of air, and has a dimension of $4 \times 4 \times 4$ m. Then the target, with its name, geometry, material, dimensions and translation is defined.
For the definition of the material, GATE provides a material database with predefined materials that can be called and altered.
For the first simulations of this thesis, a polymethyl methacrylate (PMMA) box was used as target. GATE provides a material called *PMMA*, but unfortunately it does not correspond correctly to PMMA ($C_5O_2H_8$), as it includes sulfur instead of oxygen. The correct material in the database for PMMA is called *Plastic*.

Furthermore, a physics list, containing definitions of physical processes, needs to be loaded, and a source must be defined. The source is specified by setting the particle type, energy type, shape, direction, etc. For example, it is possible to define a mono energetic proton beam with a circular shape and in the direction of x.
Either a *total number of primaries*, i.e. in our case, the number of initial protons is set, or an acquisition start and end time can be set by using a source with a defined activity.
To read the output of the simulations, the so-called *Actors* are used. Actors are tools that collect information during the simulations, but also modify their behaviour [41]. The available Actors can have diverse purposes. For the same simulation, more than one Actor can be used simultaneously.

### 3.1.2 Used Actors

The following Actors were used for this thesis.

### ProductionAndStoppingActor

The ProductionAndStoppingActor (PS-Actor) is based on the MC method. It calculates the yields based on a hadron model, which varies depending on the used physics list. For all simulations, the physics list QGSP_BIC was used. In the case of QGSP_BIC, the yields are calculated with a binary cascade model.

### CrossSectionProductionActor

The CS-Actor works differently; it is only partially based on MC. It does not use cross-section models, but calculates the production yield based on proton fluence (calculated with MC method), the energy of the protons in a voxel and cross-section data, which are provided directly in the code. The approach is based on the equation proposed by Parodi *et al* [23].
The advantages of the CS-Actor are, that it is much faster than the full-MC based PS-Actor. Therefore, an extension of the CS-Actor would be desirable, as it is currently only available for $^{11}$C and $^{15}$O.

### SimulationStatisticActor

To measure the execution time of GATE, the SimulationStatisticActor was used. This Actor does not modify the simulation, it only gathers information about the simulation and writes it into an output file. Along with other information, it shows the number of events, the number of runs and the start and end time.

#### WashOutActor

To calculate the biological washout, the OpenGATE collaboration has implemented the Mizuno model in the WashOutActor [42].
The washout effect is highly dependent on the tissue type. Therefore, to use the WashOutActor correctly the tissue was divided according to its CT Hounsfield units (HU) in five tissue types: hard bone, soft bone, fat, muscle and brain.
These tissue types were grouped in the following three components: soft bone, fat/compact bone and remaining tissue.
The WashOutActor needs the definition of a *Washout* Table in a text file, where the tissue-dependent parameters are set, namely three different decay constants ($\lambda_{f,i,s}$) and the component parameters ($M_{f,i,s}$). Therefore, for every simulated nuclide, three different sources, representing the the three tissue types, are used as input for the simulation of the washout.
The washout parameters were set according to Parodi *et al* [25].
Due to the large time delays in offline PET, in our case it is sufficient to use only the slow component of the Mizuno equation (see section 2.2.4) [29].

### 3.1.3 Modelled set-ups

To identify which $\beta^+$-nuclides need to be included in the time-resolved prediction of the PET measurement, the following $\beta^+$-emitters were chosen as candidates: $^{15}$O, $^{11}$C, $^{13}$N, $^{10}$C, $^{30}$P, $^{38}$K, $^{39}$Ca, $^{34}$Cl and $^{9}$C. However, $^{9}$C was excluded after the first simulation because its yield was almost zero.

The simulations were grouped in three set-ups:

Table 3.1: Modelled set-ups and goals

| Set-up | Goal |
|---|---|
| Simulations with a proton pencil beam and a PMMA target (140/175 MeV) | Comparing PS- and CS-Actor |
| Simulations with a proton pencil beam and a modelled human head based on a CT scan (150 MeV) | Simulate time-dependency of $\beta^+$-activity |
| Simulations with a proton therapy plan and washout | Simulate realistic therapy plan and washout |

All simulations were executed on a dedicated server located at MedAustron MedAustron server. 44 kernels were available for the simulations.

### Simulating comparison between PS- and CS-Actor

The objective of the simulations in section 4.1 was the evaluation of the relatively new CS-Actor, and its comparison to the well-established PS-Actor. The target was a $10 \times 10 \times 40$ cm$^3$ PMMA box, irradiated by a monoenergetic proton beam with 140 and 175 MeV. The shape of the beam was set to *circle*, and the radius to 0, to produce a pencil beam. The total number of primaries was set to $10^7$ protons.

### Simulating time-dependency of $\beta^+$-activity

With the simulation in section 4.2, the time- and depth-dependency of the $\beta^+$-activity after proton irradiation was analysed.
A CT scan of a patient's head was used as the target. The CT scan was available in the MetaImage format. The dimension of the scan was $346 \times 346 \times 180$ mm$^3$. The required files for importing the CT scan, like DensitiesTable or MaterialTables, were provided by the supervisor. The target was irradiated in the direction of $x$ by a mono energetic pencil beam of 150 MeV, as shown in figure 3.1.

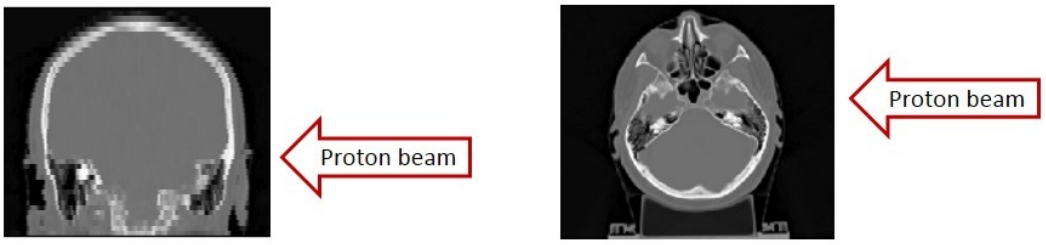


Figure 3.1: Direction of proton beam in coronal and axial plane

The calculation of the decay of the produced $\beta^+$-emitters is not included in the PS-Actor, and has to be done separately with the exponential decay formula [43]:

$$N(t) = N_0 \, e^{-\lambda t} \tag{3.1}$$

| | |
|---|---|
| $N(t)$ | Number of particles at time t |
| $N_0$ | Number of particles at time 0 |
| $\lambda$ | decay constant |
| $t$ | time |

GATE can simulate a radioactive source that decays at specific time intervals, but the decay of the secondary particles provided by the PS-Actor is not yet included. The only possibility is to start a second simulation that takes the output of the first simulation as a *voxelized source*.

For most diagrams in this set-up, an irradiation time of three minutes was assumed. During this time, $\beta^+$-emitters are simultaneously produced with the production rate, $P$, and decaying according to the radioactive decay law. For the calculation of the number of nuclides in the first three minutes, the classical decay law must be adapted. It was calculated in MATLAB with this formula for isotope production [44]:

$$N(t) = \frac{P}{\lambda}(1 - e^{-\lambda t}) \tag{3.2}$$

It should be mentioned that for the patient case, this formula is only an approximation, because the production rate $P$ is normally not constant, as the formula assumes. But for our simulation case, the energy and the material is constant, therefore it is applicable. To get $P$ the total number of produced nuclides was divided by the irradiation time.

The activity was also calculated in MATLAB with the corresponding formula [43]:

$$A(t) = N(t)\lambda \tag{3.3}$$

The simulations for $^{11}C$ and $^{15}O$ were executed with both the CS-Actor and the PS-Actor. For the rest of the $\beta^+$-emitters, only the PS-Actor was used.

### Simulating radiotherapy plan and washout

The simulations in section 4.3 were executed in two steps:

1. Simulation of the radiotherapy plan, read out yield of $\beta^+$-emitters
2. Simulation with voxelized source (containing the distribution of the $\beta^+$-emitters), read out annihilation photons

The second step is necessary to calculate the biological washout. Along with the physical decay that occurs due to radioactive decay of the nuclides, biological washout is another important process which needs to be included in predictive PET simulations.

The source of the first simulation was a realistic proton therapy treatment plan with various energy layers, depicted in figure 3.2.

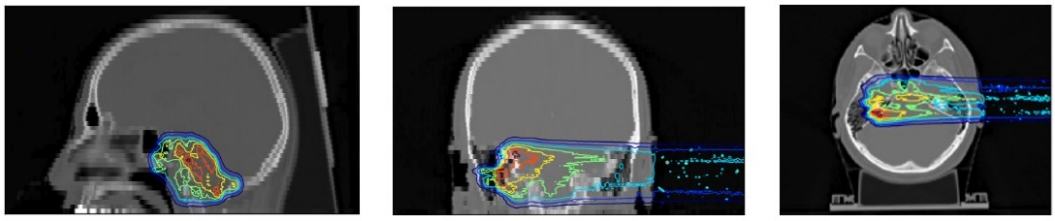

Figure 3.2: Dose distribution of the proton therapy treatment plan

The yield of the different nuclides was read out and saved as a MetaImage file. These results of the first simulation were then taken as input for the second simulation. According to the mode of operation of the WashOutActor, the output of the first simulation had to be split in three sources for each nuclides, and then used as voxelized sources (see section 3.1.2).
In the second simulation the annihilation photons following the $\beta^+$-activity, and not the yield of the $\beta^+$-emitters, were read out with the

PS-Actor.

The PS-Actor produces two output files, a *Prod* and a *Stop* file. The Prod file tells where the particle was produced, and the Stop file where it is stopped in the tissue. For the previous simulations, the Stop file was used, as the movement of the target fragments is negligible.
In the case of reading out photons, the Prod files must be used to obtain the activity of the patient, because photons will most likely leave the target.
The simulations with the radiotherapy plan were done exclusively with the PS-Actor, because at the moment, the CS-Actor is only available for $^{11}$C and $^{15}$O. To ensure comparability, the PS-Actor was used for all nuclides.
To include the biological washout, the WashOutActor was used.

The manipulation of the MetaImage files and the visualisation of the 3D data were done with Python. A Gaussian filter with $sigma = 1$ was applied on the 3D visualisations to smooth them. The 1D profiles were visualised with MATLAB.
In this group of simulations, only $^{11}C$, $^{15}O$, $^{13}N$, $^{30}P$ and $^{38}K$ were included. Based on the findings of the previous simulations, $^{11}C$, $^{15}O$ and $^{13}N$ were included because of their high yield. $^{30}P$ and $^{38}K$ were included because they represent $\beta^+$-emitters in bony structures, tissue with low washout. The idea was to examine if they gain influence after incorporating the washout effect.

Figure 3.3 depicts the workflow and processes during proton therapy, and the corresponding simulation in GATE.

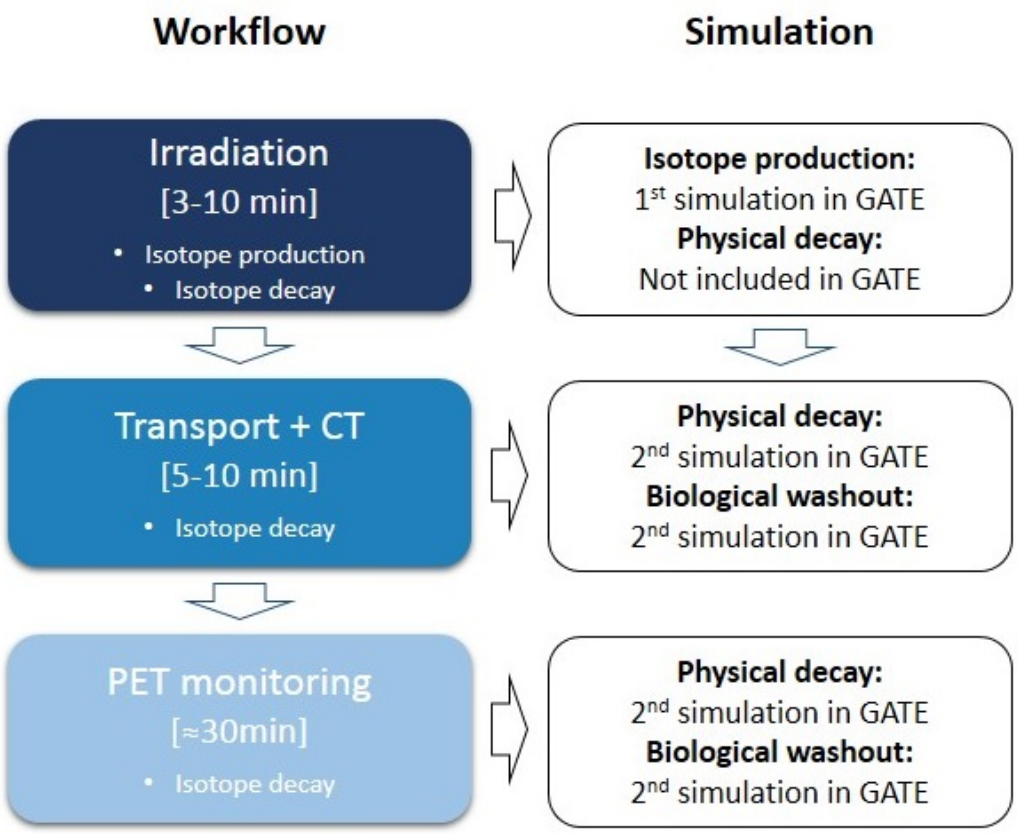


Figure 3.3: Workflow of proton therapy and simulation

This two-step approach was already proposed by Jan *et al* [28].
At the moment, it is the only way to include the biological washout in GATE. Since the second simulation was needed anyway, the physical decay, which was previously calculated by MATLAB, was enabled in the GATE macros.
This two-step approach is actually beneficial for the clinical routine. The first step starts with the CT acquisition of the patient and the treatment planning. The execution time for the first simulation is much longer than for the second. However, there is one week in which to

perform the first simulation between the treatment planning and the actual irradiation.. The second simulation has to be much faster, as it is performed right after the irradiation, with the actual irradiation time and transport time. If the results of the first simulations are already available, the second step, the simulation of washout and physical decay, can be performed really fast [28].

## 3.2 Analysis with MATLAB

The 1D depth-dependent profiles were generated using MATLAB.
The output of the simulations was written into text files by GATE. For every used kernel, one text file with one row was created. These text files were summed up to one 1D matrix, and plotted with MATLAB.
For the time-dependent modelling the $\beta^+$-activity, the data acquired from GATE was manipulated by integrating and applying the aforementioned exponential decay formula, as well as the formula for radioactive activity and isotope production.
In order to visualise the overall yields at different times (figure 4.16), at first, for every point of time, the yield of every nuclide was calculated separately. Then, all nuclide yields in every point of time were summed up, and written into a new text file. The values of these text files were plotted.

Also several calculations were done in MATLAB. The overall yield in table 4.1 and the deviation values in table 4.2 were calculated with the *trapz* method in MATLAB.

## 3.3 Occurred problems in the simulations

During the simulations, some particularities and problems in GATE were discovered.

In the depth-dependant diagrams of section 4.2.3, a discrepancy occurred between the CS-Actor and PS-Actor. The discrepancy only exists for the yield of $^{15}O$, and especially, at areas with HU of zero (water, soft tissue). Further examination of this discrepancy is needed.

During the simulations with the proton pencil beam (in section 4.2), a bug in the CS-Actor was detected. The simulations were executed in both the $x$- and $z$-directions, although only the simulations in $x$ were used for the evaluations. In the direction of $z$, the results of the CS-Actor were reasonable, but in the direction of $x$, the results were many times higher than the results of the PS-Actor.
It was discovered by my supervisor, Heide Rohling, that the CS-Actor always assumes a beam in $z$-direction when it performs a division by the length of the voxels in beam direction. In our case, a workaround was used to avoid the bug. The results of the actor were divided by the size of the voxels in dimension $z$.

Another oddity about the CS-Actor is the fact that the command *addC11* can only have the value *true*. If the value is set to *false*, the simulation does not work. So it is not possible to read out only $^{15}O$ by setting *addO15* to *true*, because it will always simulate $^{11}C$ as well.

## 3.4 Used macros and files

Many GATE macros and some Python scripts were provided by Heide Rohling, and then altered and extended for this thesis.

For all set-ups, existing GATE macros with the basic structures were provided. These GATE macros were adapted and extended for all needed nuclides. This is also the case for the definitions of the used Actors and the voxelized sources.
In the third set-up, a Python script for the splitting up of the sources was provided and used with some optimisations.
Another existing Python script for the visualisation of the 3D data was altered and optimised.
Further, the washout table and the rangetranslator file from Heide Rohling were used without changes.

The simulated data of the first set-up, the irradiation of a PMMA box, were compared to experimental data of the Helmholtz-Zentrum Dresden-Rossendorf, Institute of Radiation Physics, Department of Radiation Physics [23].

The proton therapy plan was provided by Hermann Fuchs from the Medical University of Vienna. The files for the therapy plan and the imported CT scan with material conversion were complete and ready to use.

# 4 Results and discussion

The following chapter presents and discusses the results obtained by the performed GATE simulations.

## 4.1 Applicability and accuracy of the CrossSectionProductionActor

The CS-Actor was evaluated regarding its accuracy, execution time and required resources.

### 4.1.1 Comparison of the PS-Actor and the CS-Actor

To evaluate the accuracy of PS- and CS-Actor, the results obtained with these two actors were compared to experimental data (see section 3.4), as depicted in figures 4.1 and 4.2.
A PMMA box was irradiated by a proton beam with 140 and 175 MeV. The range of protons in PMMA is 12.16 cm for 140 MeV and 17.93 cm for 175 MeV [45].

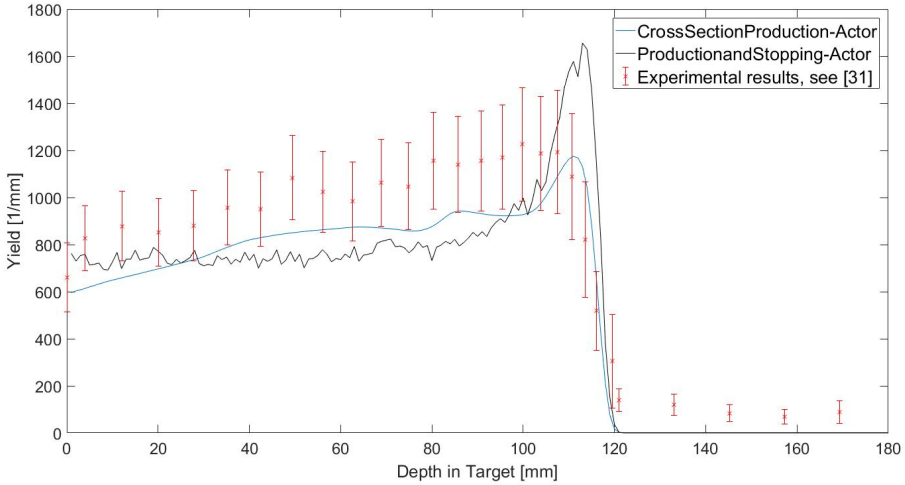


Figure 4.1: Depth-dependent production of $^{15}O$ resulting from proton irradiation (140 MeV, $10^7$ protons) of a PMMA target

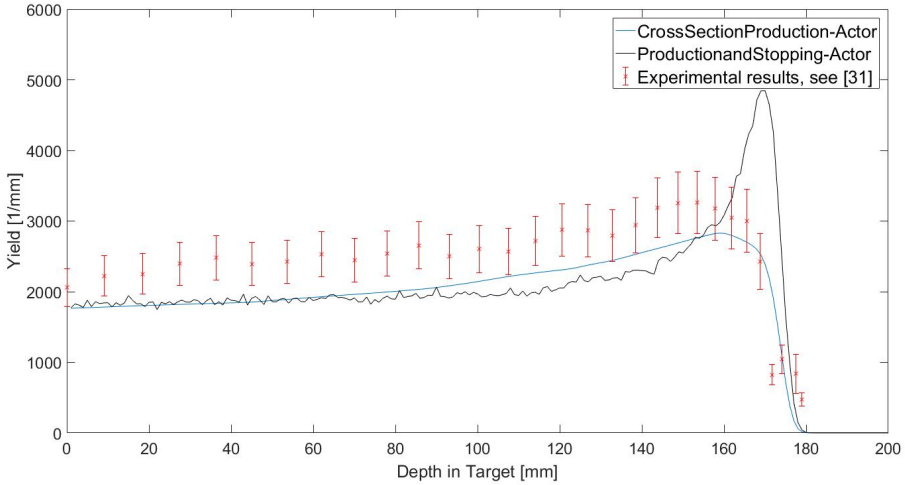


Figure 4.2: Depth-dependent production of $^{11}C$ resulting from proton irradiation (175 MeV, $10^7$ protons) of a PMMA target

By only comparing the overall yields (the experimental data and the simulation data were integrated with the trapezoidal method, the values were verified by comparing them to Pschenichnov *et al* [27]), the PS-Actor would seem to be more accurate because the CS-Actor underestimates the overall yields more than the PS-Actor (Table 4.1). However, figures 4.1 and 4.2 show that the CS-Actor corresponds better to the shape of the experimental curve than the PS-Actor, for $^{15}$O as well as for $^{11}$C. In the plateau, both actors have similar values, but because of the high peak in the PS-Actor data, which does not exist in the experimental data, the underestimated values at the other depths are balanced out.

Table 4.1: Overall yields and differences of the results obtained with the PS- and CS-Actor compared to the experimental data (proton beam, PMMA box as target)

| Simulation | Experimental data | PS-Actor | CS-Actor |
|---|---|---|---|
| $^{11}$C, 140 MeV | 336430 | 290534 (-14.64%) | 281692 (-16.27%) |
| $^{11}$C, 175 MeV | 453552 | 382946 (-15.75%) | 371736 (-18.04%) |
| $^{15}$O, 140 MeV | 122984 | 99013 (-19.49%) | 97846 (-20.44%) |
| $^{15}$O, 175 MeV | 158479 | 135080 (-14.76%) | 123698 (-21.95%) |

### 4.1.2 CS-Actor with different proton quantities

A major advantage of the CS-Actor is the shorter execution time, because it needs less proton quantities than the PS-Actor to calculate an accurate simulation. To find the best compromise between proton quantity and execution time, several simulations with different proton quantities were compared.

Table 4.2 depicts this quantitative analysis for proton irradiation of a PMMA target. The percentage of the deviation between the simulation with $10^8$ protons (as a pretty accurate base), and the other simulations from $10^2$ to $10^7$ protons was calculated. The deviation is a mean point wise deviation. Only points where the function (yield) of $10^8$ protons is $> 1$ were considered (until the depth of 180 mm). $10^8$ protons were taken as basis because the results do not change considerably with higher proton quantities. The numbers refer to the yield of $^{11}C$.

In tables 4.3 and 4.4 the execution times for proton irradiation of a CT head target with a proton pencil beam and a radiotherapy plan are listed. In all tables the execution time was provided by the SimulationStatisticActor in GATE. The execution time is dependent on the energy. The radiotherapy plan consists of various energy levels, all of them are lower than 150 MeV. That is why the execution time of the radiotherapy plan can be lower than the one with the monoenergetic 150 MeV proton pencil beam.

Table 4.2: Deviations and execution times of CS-Actor simulations with different proton quantities, PMMA box, 175 MeV

| Proton quantity | Deviation | Execution time/ kernel [min] |
|---|---|---|
| $10^2$ | 3.9750% | 0.02 |
| $10^3$ | 1.7843% | 0.03 |
| $10^4$ | 0.5885% | 0.2 |
| $10^5$ | 0.2363% | 1.93 |
| $10^6$ | 0.1344% | 18.53 |
| $10^7$ | 0.0283% | 176 |
| $10^8$ | - | 1.680 (28h) |

Table 4.3: Execution times of CS-Actor simulations with different proton quantities, Proton pencil beam, Patient CT, 150 MeV

| Proton quantity | Execution time/ kernel [min] |
|---|---|
| $10^2$ | 0.25 |
| $10^3$ | 2.06 |
| $10^4$ | 20 |
| $10^5$ | 200 |
| $10^6$ | 2.200 (36h) |
| $10^7$ | 21.600 (360h) |
| $10^8$ | 216.000 (3600h) |

Table 4.4: Execution times of CS-Actor simulations with different proton quantities, radiotherapy plan with 1 energy layer, Patient CT

| Proton quantity | Execution time/ kernel [min] |
|---|---|
| $10^2$ | 0.21 |
| $10^3$ | 1.55 |
| $10^4$ | 16.6 |
| $10^5$ | 152 |
| $10^6$ | 1.600 (26h) |
| $10^7$ | 14.400(240h) |
| $10^8$ | 144.000(2380h) |

Figure 4.3 illustrates a comparison of the curves with different proton quantities. The curves were multiplied with a multiple of 10 to overlap with the curve of the simulation with $10^8$ protons

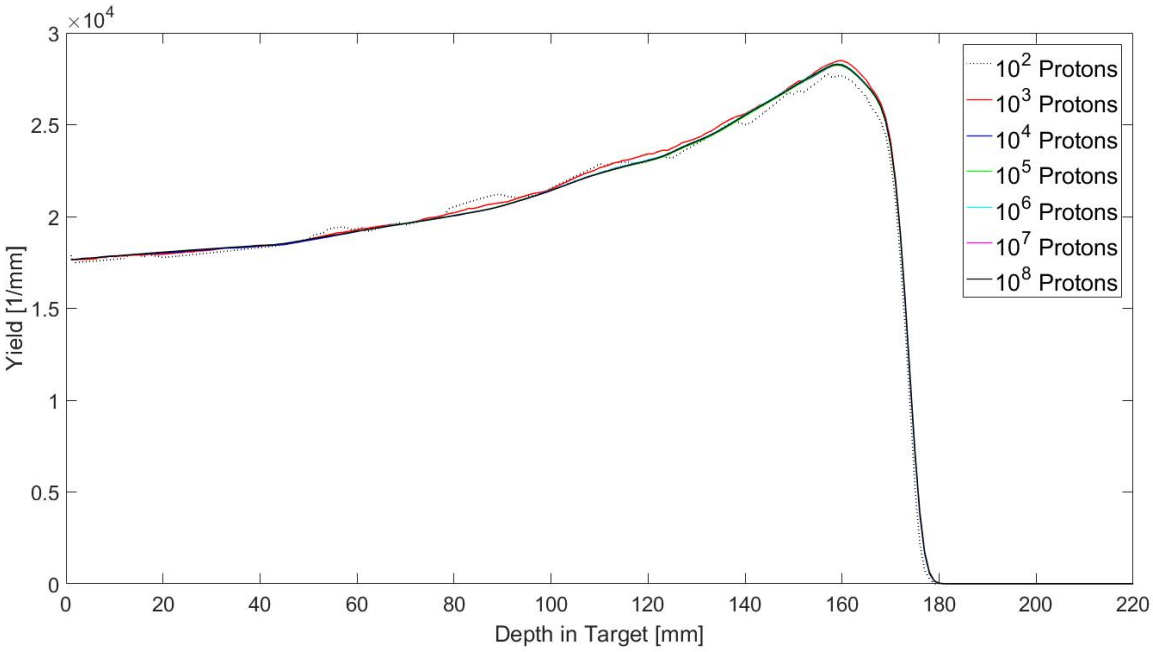


Figure 4.3: Comparison of CS-Actor simulations with different proton quantities, PMMA box, 175 MeV, $^{11}C$

In figure 4.4 the functions of the simulations were normalized to the curve of the simulation using $10^8$ protons. After the depth of approx. 175 mm, the deviation curve is distorted because of small values that can easily lead to a high deviation in percentage (but still insignificantly small in absolute numbers).

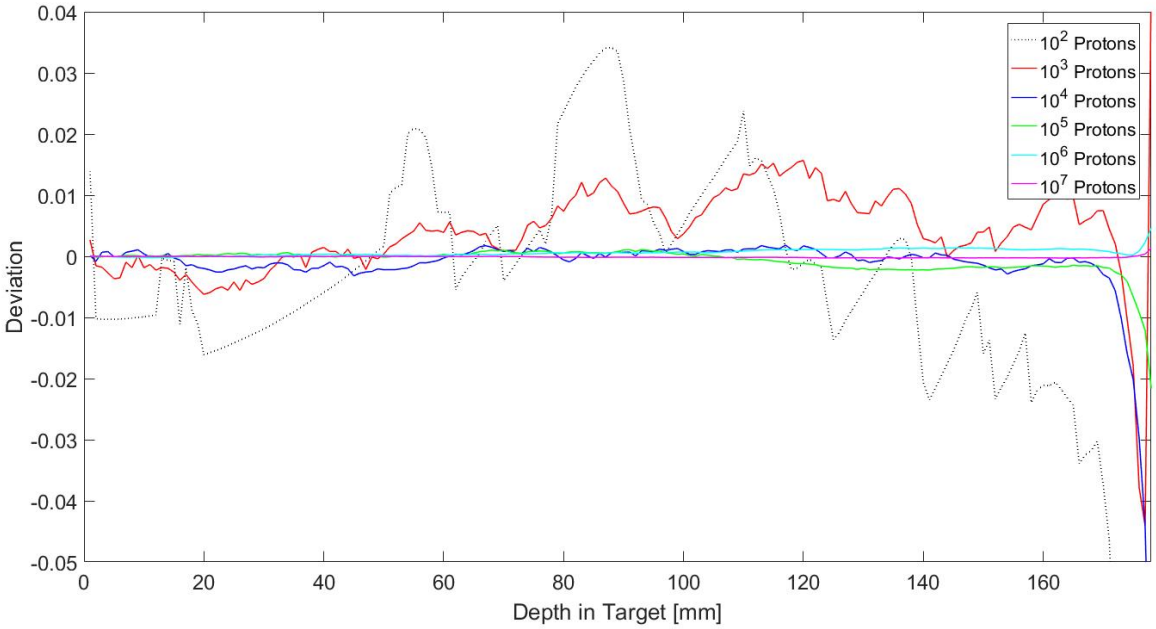


Figure 4.4: Relative deviations of the simulation values with different proton quantities in reference to the $10^8$ curve, PMMA box, 175 MeV, $^{11}C$

Both the graphic and quantitative analysis indicate that $10^4$ protons seem to be enough to simulate with the CS-Actor. The mean point wise deviation for $10^4$ is already under 1%. In the graphical analysis, all curves with higher quantities than $10^4$ and the curve of $10^4$ protons are close to each other.

## 4.2 Time-dependent modelling of $\beta^+$-activity

For the following simulations, a patient head CT was imported into GATE, and irradiated with a proton pencil beam.

### 4.2.1 Number of considered $\beta^+$-emitters over time

Table 4.5 lists the total amount of produced $\beta^+$-emitters according to the GATE simulations.

Table 4.5: Number of produced $\beta^+$-emitters in GATE, 150 MeV, proton beam, $10^7$ protons, patient head CT

| Nuclide | Half-life[min] | Number of produced nuclides |
|---|---|---|
| $^{15}$O | 2.032 | 192.538 |
| $^{11}$C | 20.383 | 190.986 |
| $^{13}$N | 9.967 | 29.973 |
| $^{10}$C | 0.317 | 22.716 |
| $^{38}$K | 7.633 | 8.815 |
| $^{30}$P | 2.500 | 8.436 |
| $^{39}$Ca | 0.014 | 5.660 |
| $^{34}$Cl | 0.025 | 3.578 |

The number of $\beta^+$-emitters over time looks fairly different, depending on whether the irradiation time is considered or not. The output file of the GATE simulation contains the total number of produced nuclides at various depths. At first, these total numbers of production were

visualised only with the inclusion of the radioactive decay, which was manually calculated with MATLAB. The irradiation time was not included, so it was assumed that all nuclides were produced at once before time 0. Later, the irradiation time was included using MATLAB, as described in section 3.2. It was seen that the irradiation time is not negligible.
Figure 4.7 depicts the number of $\beta^+$-emitters without considering irradiation time and figures 4.5 and 4.6, with the assumption of an irradiation time of three minutes. In figure 4.6, the lower part of figure 4.5 is depicted with an enlarged viewing. It can be seen that nuclides with short half-lives, like $^{15}$O, are overestimated if the decay during irradiation is not taken into consideration.

The total amount of produced $^{15}$O is as high as the total amount of produced $^{11}$C (table 4.5), but $^{15}$O decays quickly ($T_{1/2}$=2,03 minutes). After the irradiation, more than an entire half-life has already past. This is why $^{11}$C is the most dominant nuclide, as can be seen in figure 4.5. Right after the irradiation, the yield of $^{13}$N is far lower than $^{15}$O and $^{11}$C, but after 7 minutes, it passes $^{15}$O and becomes the second most frequent nuclide. The fourth most frequent nuclide is $^{38}$K, due to its rather long half-life ($T_{1/2}$=7,63 minutes). After irradiation, the yield of $^{30}$P is comparable to $^{38}$K, but at the beginning of the PET monitoring (approximately minute 15), it is already irrelevant. $^{10}$C starts with a yield that is comparable to $^{30}$P, but it decays quickly, and is already insignificant after the irradiation. $^{39}$Ca and $^{34}$Cl are negligible from the start because their half-lives are less than one second. $^{9}$C is not included because its yield is almost zero.

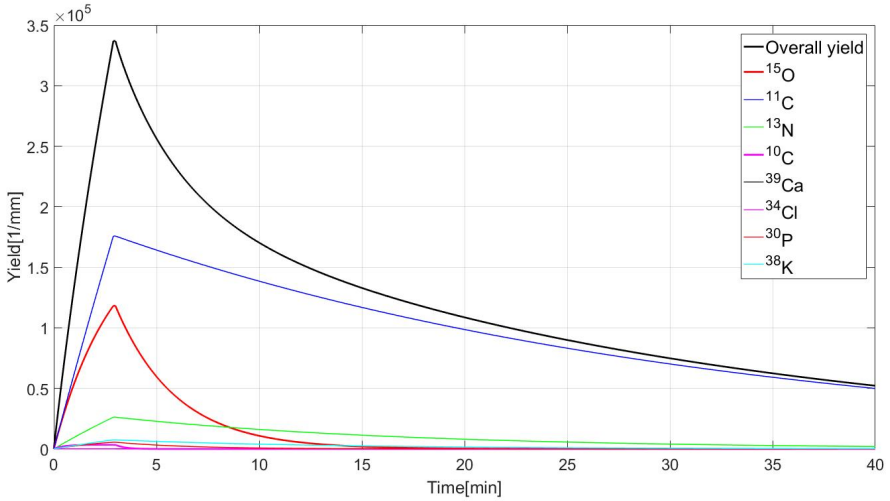


Figure 4.5: Number of $\beta^+$-emitters over time, 150 MeV, proton beam, $10^7$ protons, patient head CT, assuming three minutes irradiation time

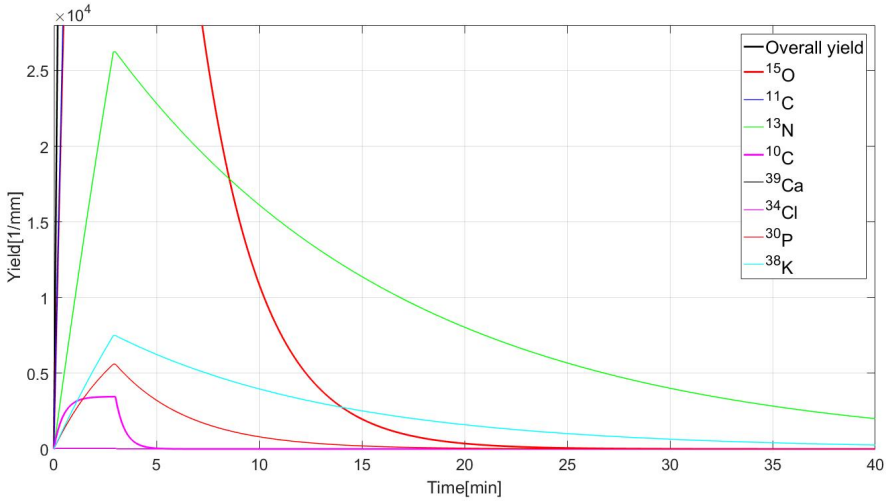


Figure 4.6: Number of $\beta^+$-emitters over time, lower part, 150 MeV, proton beam, $10^7$ protons, patient head CT, assuming three minutes irradiation time

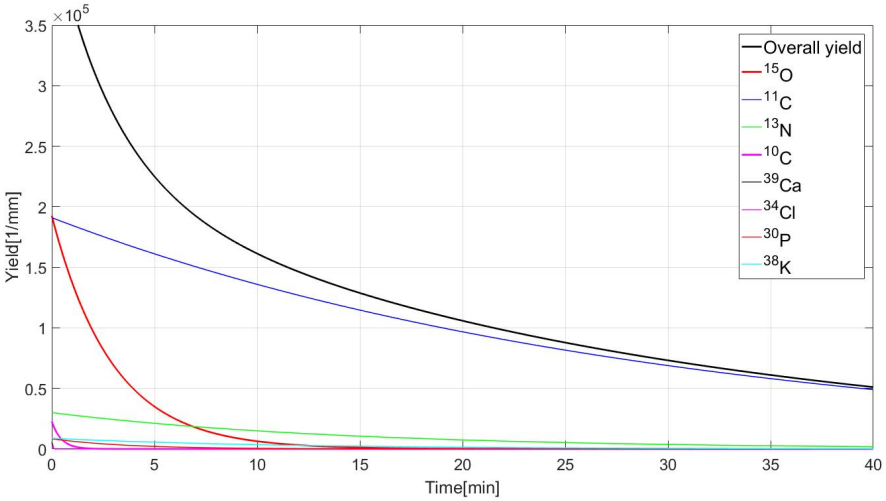


Figure 4.7: Number of $\beta^+$-emitters over time, 150 MeV, proton beam, $10^7$ protons, patient head CT, irradiation time set to 0

The percentage of $\beta^+$-emitters over time is depicted in figure 4.8. After 1 minute, $^{15}$O still represents 40.5%, and $^{11}$C, 46% of the yield at that time. The percentage of remaining $^{13}$N equals 7.1%, and the other nuclides ($^{30}$P, $^{39}$Ca, $^{34}$Cl, $^{38}$K, $^{10}$C) constitute the remaining 6.4% of the overall yield.
After 5 minutes, $^{13}$N already reaches 8.9%. $^{11}$C is the most dominant nuclide with 63.6%, and $^{15}$O decreased to 23.9% of the overall yield. The other nuclides make up the remaining 3.7%.
After 10 minutes, $^{11}$C represents a large majority of the overall yield, 81.1%. $^{15}$O is reduced to only 6.6%. $^{13}$N overtakes $^{15}$O with 9.5%. The other nuclides make up 2.8%.
After 30 minutes, almost all nuclides are insignificant in comparison to $^{11}$C, which represents 93.7% of the overall yield. Only $^{13}$N has a certain significance, with 5.4% of the overall yield. $^{15}$O decreased to 0%, and the other nuclides make up only 0.9%.

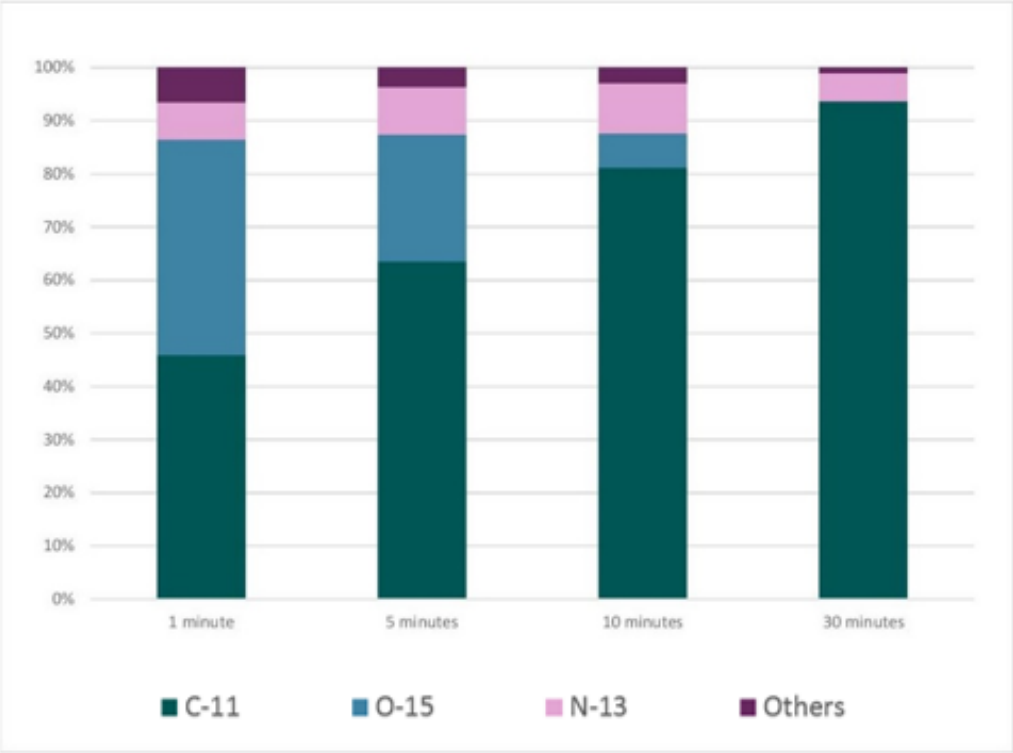


Figure 4.8: Percentage of $\beta^+$-emitters over time, 150 MeV, proton beam, $10^7$ protons, patient head CT, assuming three minutes irradiation time

### 4.2.2 Activity of considered $\beta^+$-emitters over time

Figure 4.9 represents the activity over time. Figure 4.10 shows the lower part of the curves with an enlarged viewing.
For these diagrams, again an irradiation time of three minutes was assumed and included in the diagrams. As expected, the activity of $^{15}O$ is the highest due to its short life-time. Especially for in-beam or in-room PET, modalities with short transport time, it can be seen that the activity of $^{15}O$ is relevant. From minute 5 to minute 15, 59.808

$^{15}$O-nuclides decay. During offline PET monitoring, from minute 10 to 40, only 11.249 $^{15}$O decay. $^{10}$C has relatively high activity during the irradiation time, but it falls to almost zero within one minute. $^{11}$C has a relatively constant activity. After nine minutes, it is the nuclide with the highest activity. After 15 minutes, at the beginning of the offline PET monitoring, $^{13}$N has the second highest activity. $^{30}$P and $^{38}$K also have some mentionable activity in the first 15-20 minutes. The activity of $^{39}$Ca and $^{34}$Cl falls to zero immediately after the irradiation time.

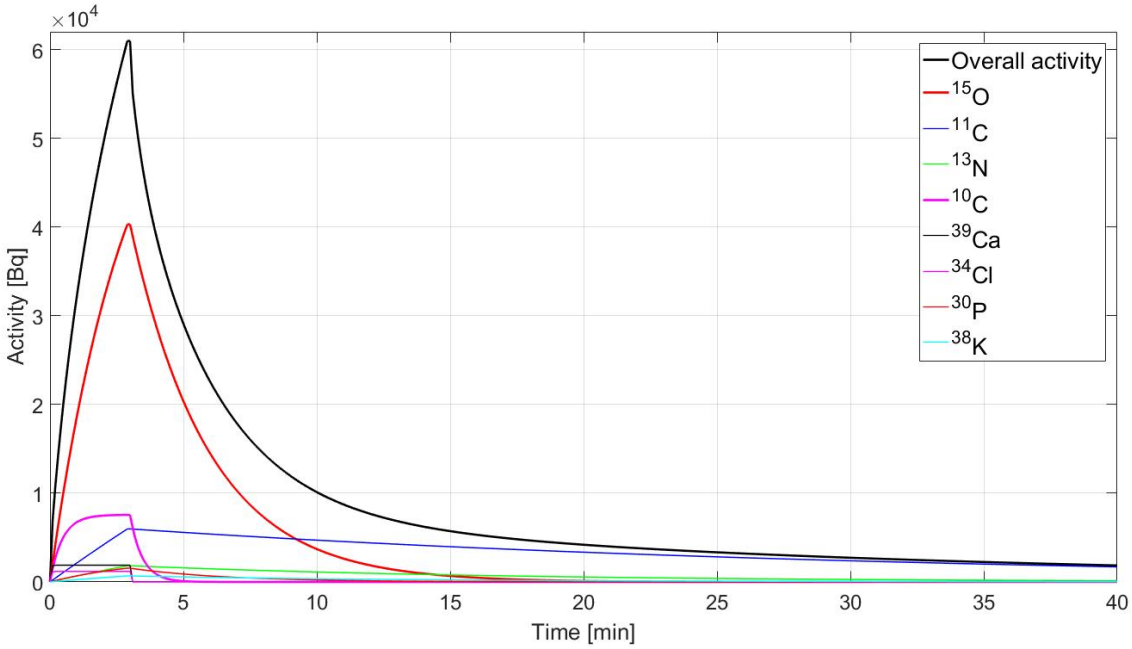


Figure 4.9: Activity of $\beta^+$-emitters over time, 150 MeV, proton beam, $10^7$ protons, patient head CT, assuming three minutes irradiation time

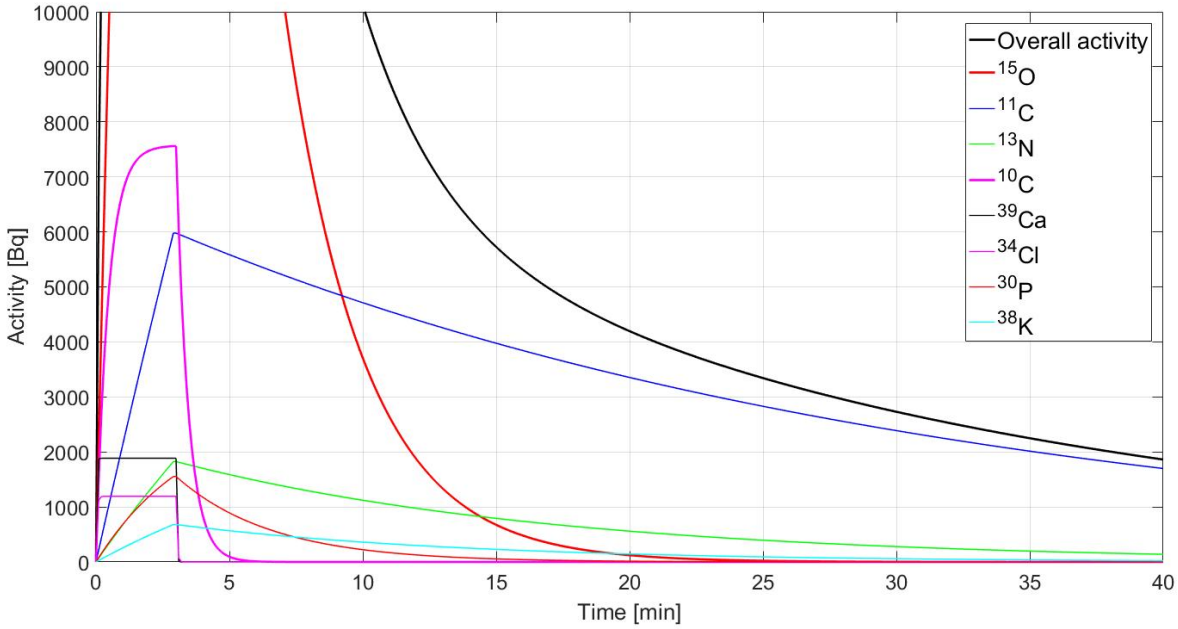


Figure 4.10: Activity of $\beta^+$-emitters over time, lower part, 150 MeV, proton beam, $10^7$ protons, patient head CT, assuming three minutes irradiation time

### 4.2.3 Depth-dependent amounts of $\beta^+$-emitters

Figure 4.11 shows the distribution of $^{15}O$ in the depth of the target. A discrepancy can be observed between the CS-Actor and PS-Actor especially at areas with HU of zero (water, soft tissue). Further examination of this discrepancy is needed.

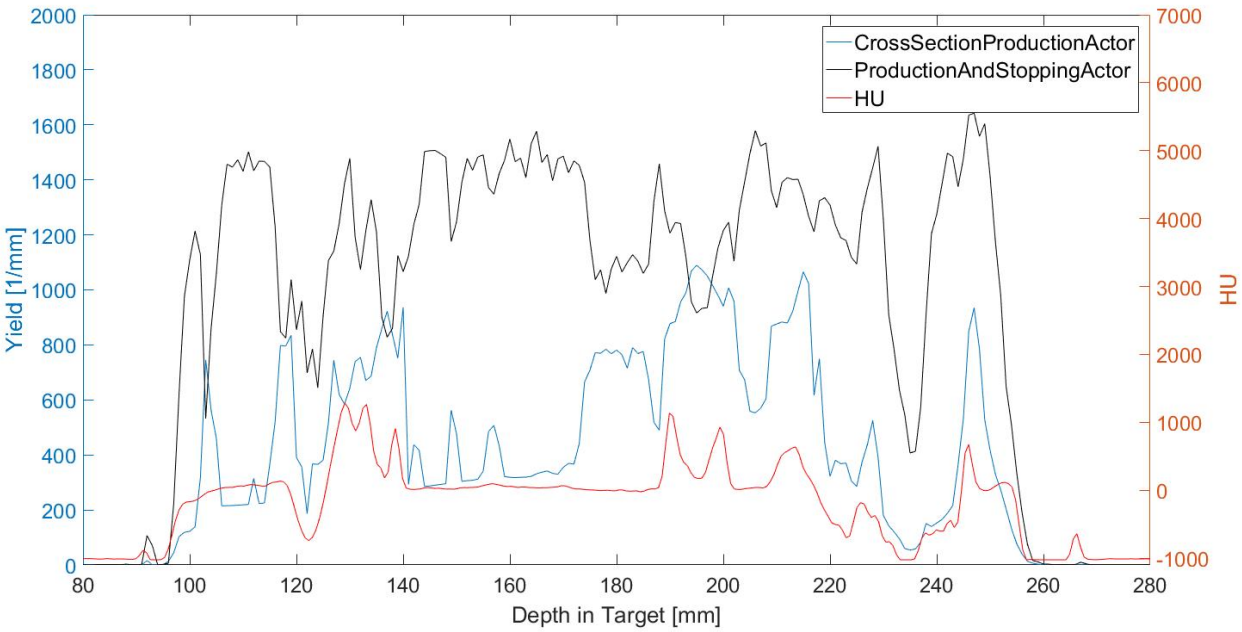


Figure 4.11: Depth-dependent distribution of $^{15}O$, 150 MeV, proton beam, $10^7$ protons, patient head CT

In the case of $^{11}$C (figure 4.12), there is no huge discrepancy between CS- and PS-Actor, as in the case of $^{15}$O. However, the CS-Actor shows lower yields, especially at the depth with HU zero. In general, it can be said that the yield of $^{11}$C tends to be high with high HU (e.g. bone).

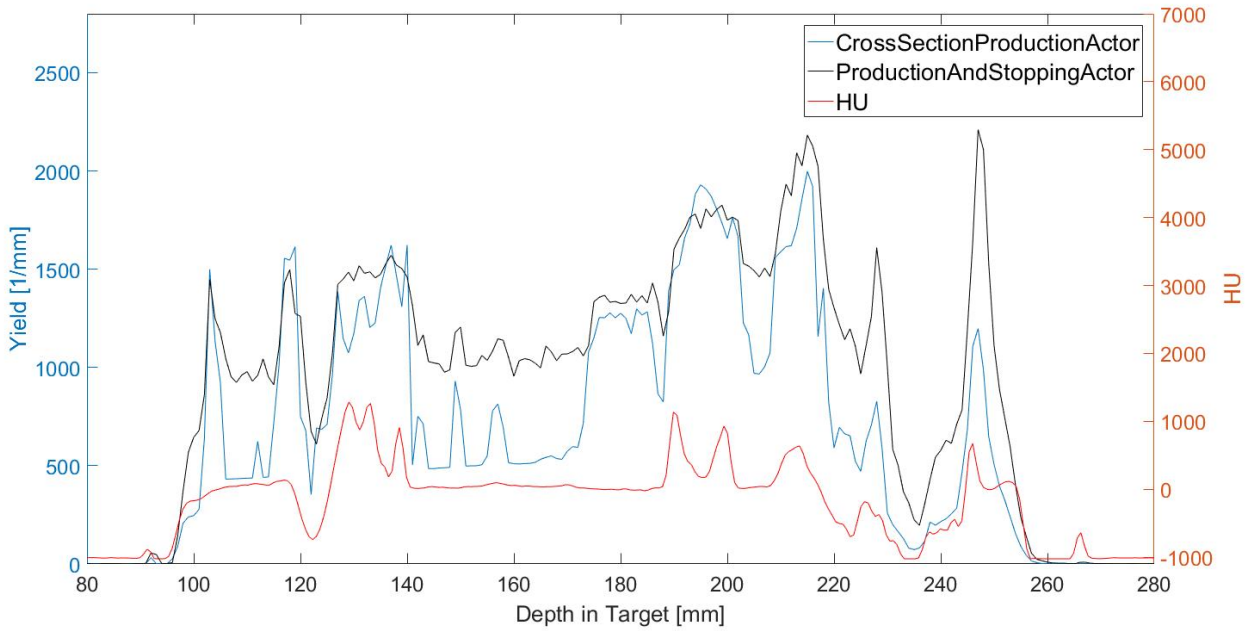


Figure 4.12: Depth-dependent distribution of $^{11}$C, 150 MeV, proton beam, $10^7$ protons, patient head CT

Figure 4.13 shows the distribution of $^{13}$N. In contrast to $^{15}$O and $^{11}$C, the yield of $^{13}$N is also relatively high in the areas with HU zero. This could be a result of the nuclear reactions which produce $^{13}$N out of $^{16}$O.

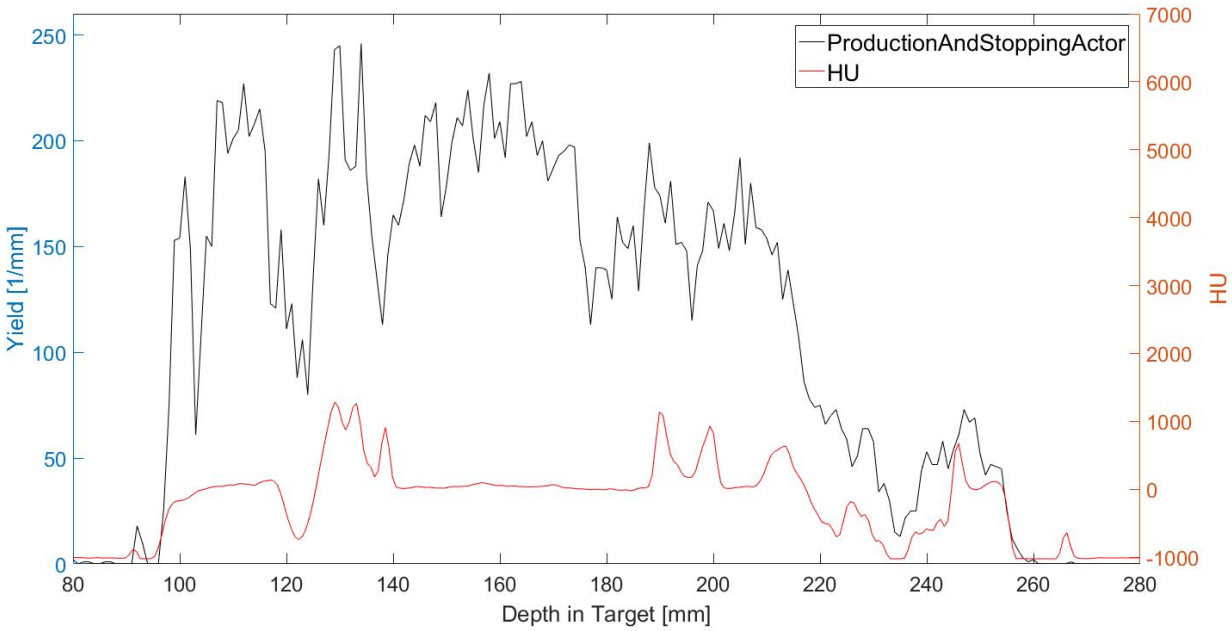


Figure 4.13: Depth-dependent distribution of $^{13}$N, 150 MeV, proton beam, $10^7$ protons, patient head CT

Figure 4.14 depicts an overview of the depth-dependent distributions of all considered $\beta^+$-emitters in comparison to the overall yield. Figure 4.15 represents the lower part of the diagram.

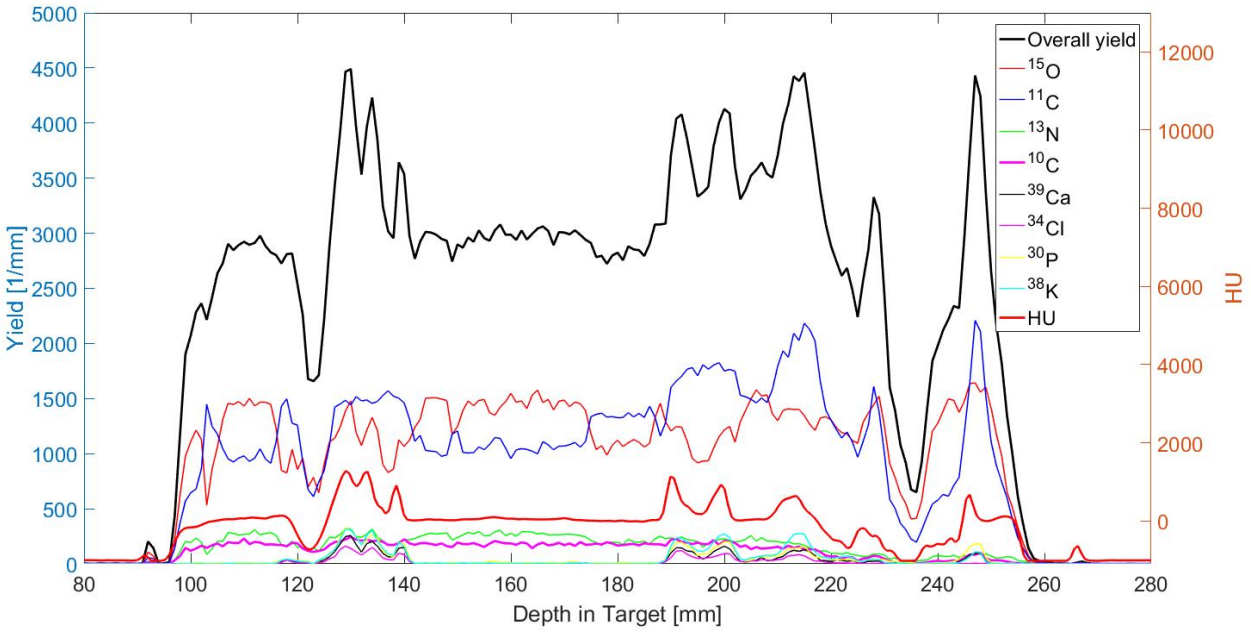


Figure 4.14: Depth-dependent distribution of all considered nuclides, 150 MeV, proton beam, $10^7$ protons, patient head CT

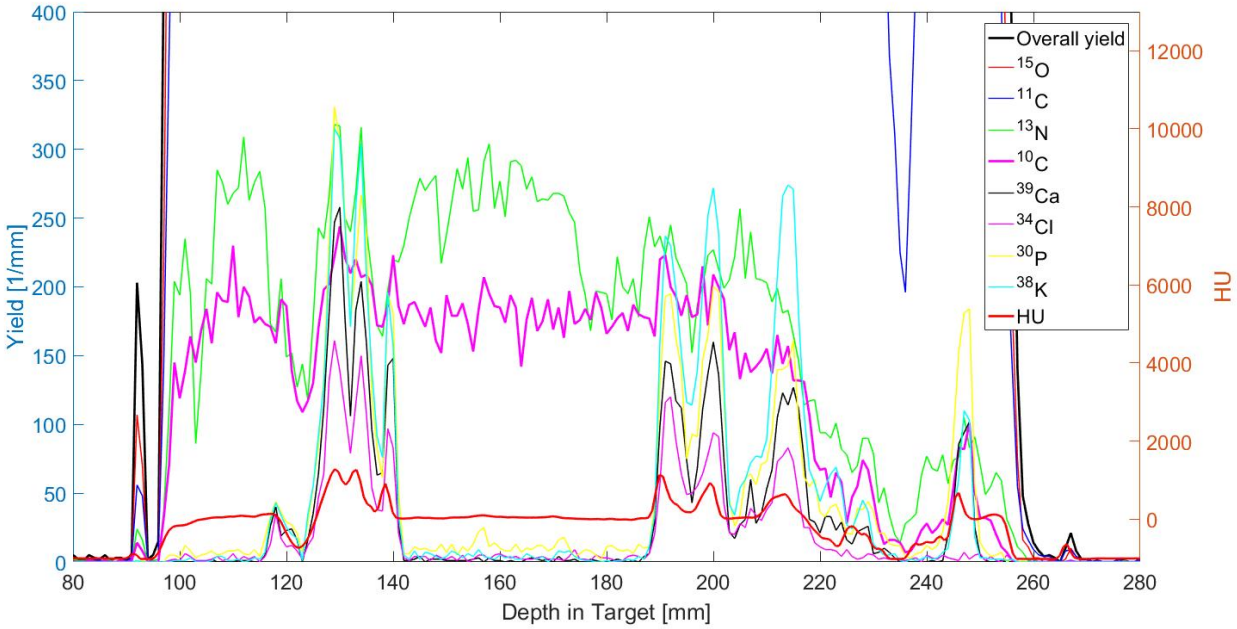


Figure 4.15: Depth-dependent distribution of all considered nuclides, lower part, 150 MeV, proton beam, $10^7$ protons, patient head CT

In figure 4.16, a comparison of the summed curves of all examined $\beta^+$-emitters after different time periods can be seen. Irradiation time was not considered in this case, only physical decay. The curves were normalized, and then multiplied with the sum of all points of the curve of Minute zero, to allow for a better comparison of the shapes of the different curves.
It can be observed that the depth-distribution changes with time. The values at the areas with high HU become higher with time, at HU equal to water/soft tissue they get lower. As already shown, the dominance of $^{11}$C increases with time, so the shape of the overall yield is converging towards the shape of the yield of $^{11}$C. $^{11}$C has a higher yield at areas of high HU.

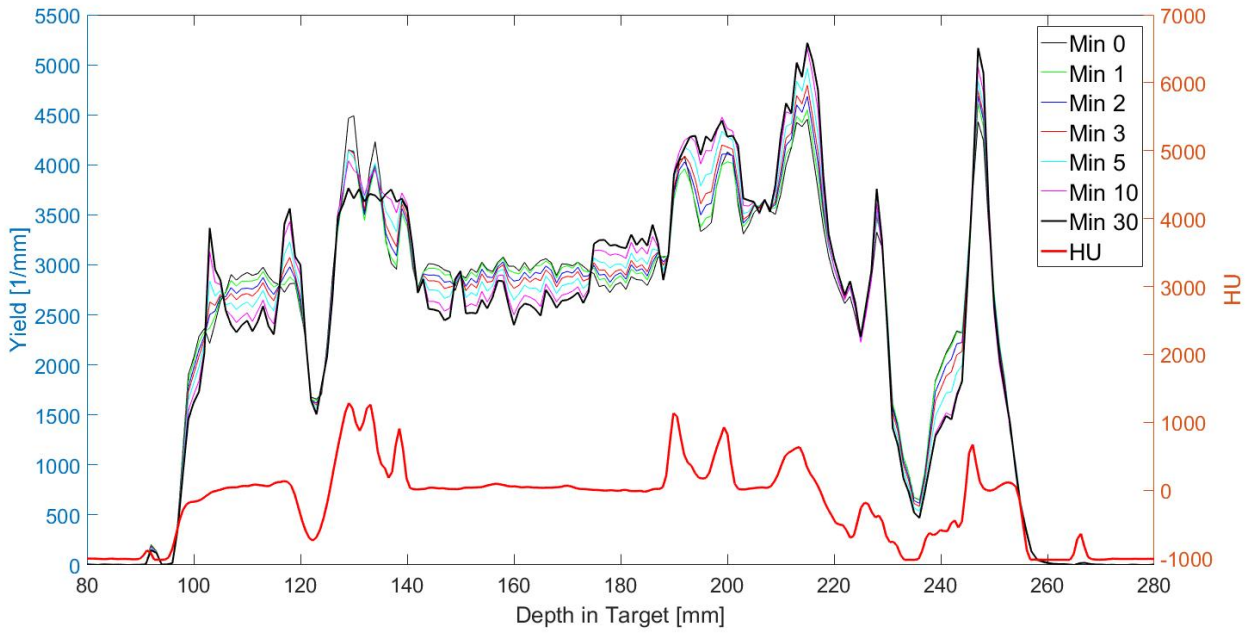


Figure 4.16: Normalized overall yields at different times, 150 MeV, proton beam, $10^7$ protons, patient head CT, without considering irradiation time

## 4.3 Simulations with radiotherapy plan and washout

The radiotherapy plan was first simulated without washout, and then with washout effect. The washout effect was modelled according to the Mizuno model described in section 3.1.2. To simulate the washout, the source is divided in three regions with low, intermediate and normal perfusion, based on their HU, see figure 4.17. The parameter for soft bone, remaining tissue and fat/compact bone were set as follows: $\lambda_s$ to 8.000,10.000 and 15.000 seconds; $M_s$ to 0.6, 0.35 and 0.9.

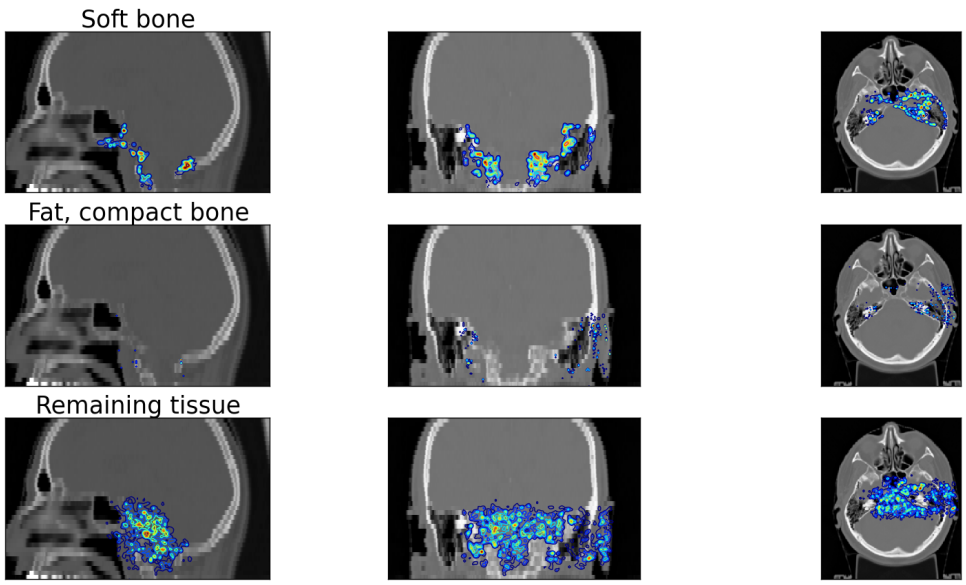


Figure 4.17: Split $^{11}$C source according to the HU of the corresponding tissue. Top: Soft bone, Centre: Fat, compact bone, Bottom: Remaining tissue

These split sources were used as voxelized sources for the second simulation which includes the WashOutActor in GATE, and reads out the produced photons.

### 4.3.1 Activity during PET monitoring

Figures 4.18, 4.19 and 4.20 represent the activity of selected $\beta^+$-emitters during offline PET monitoring, i.e. all photons that were emitted during the monitoring. The time period was set from 10 to 40 minutes, assuming the PET monitoring takes place in this time period. At the

moment, it is still not possible to include the irradiation time in the GATE workflow. Therefore, the irradiation time is not considered in the simulations of this set-up.
The colours of the figures are only a representation of the relative distribution of annihilation photons of one specific nuclide. They should primarily show the location of the different $\beta^+$-emitters and not the total amount. The colours can be compared for the same nuclide but not between the nuclides. Therefore, the amount of $^{15}O$ in figure 4.18 seems higher than the amount of $^{38}K$ in figure 4.20, although the total amount of $^{38}K$ is higher, but only more concentrated in smaller areas.

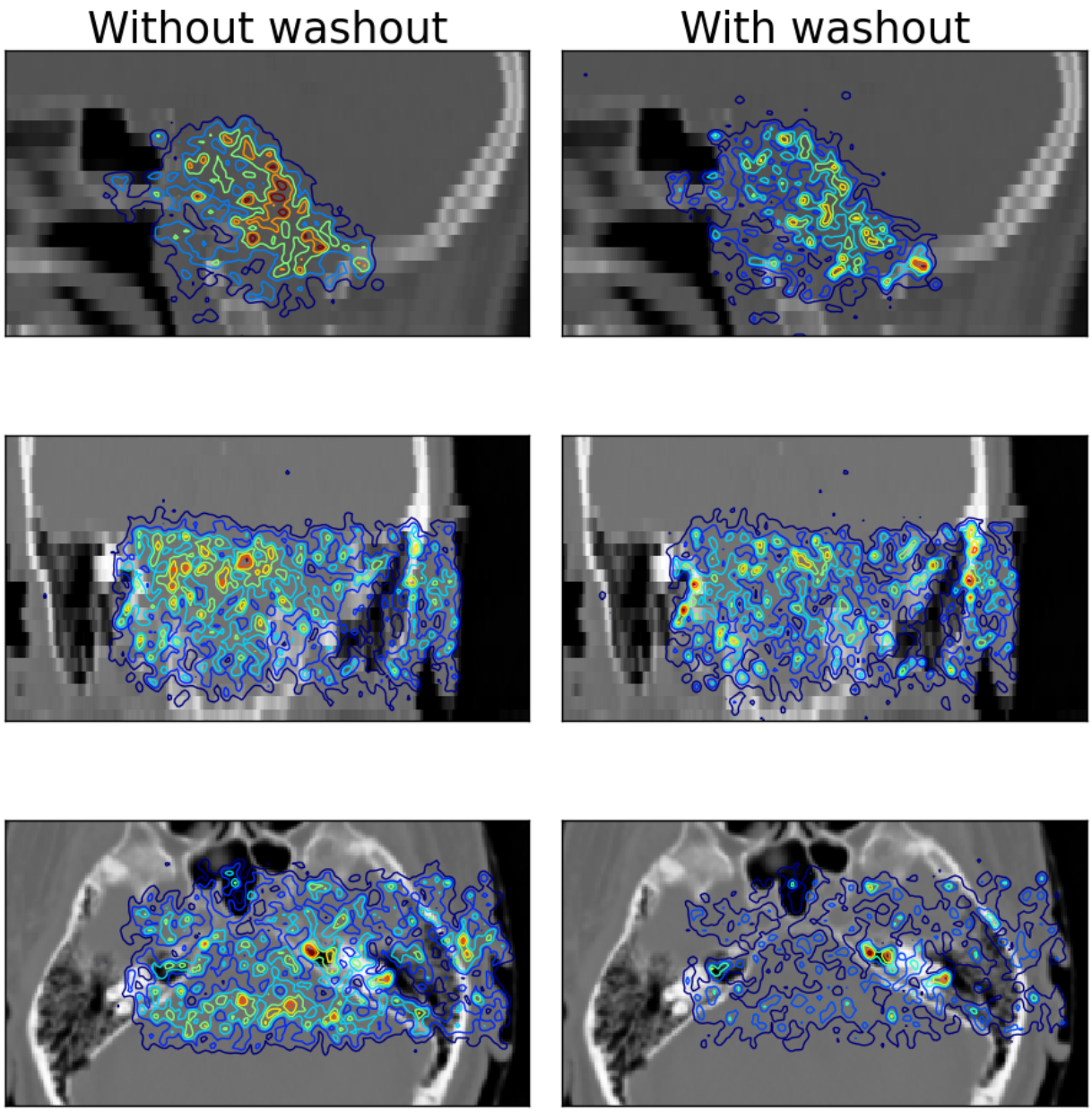


Figure 4.18: Annihilation photons following the decay of $^{15}O$ with and without Washout, time set from minute 10 to 40, radiotherapy plan, $10^7$ protons, patient head CT. Top: Without washout, Bottom: With washout

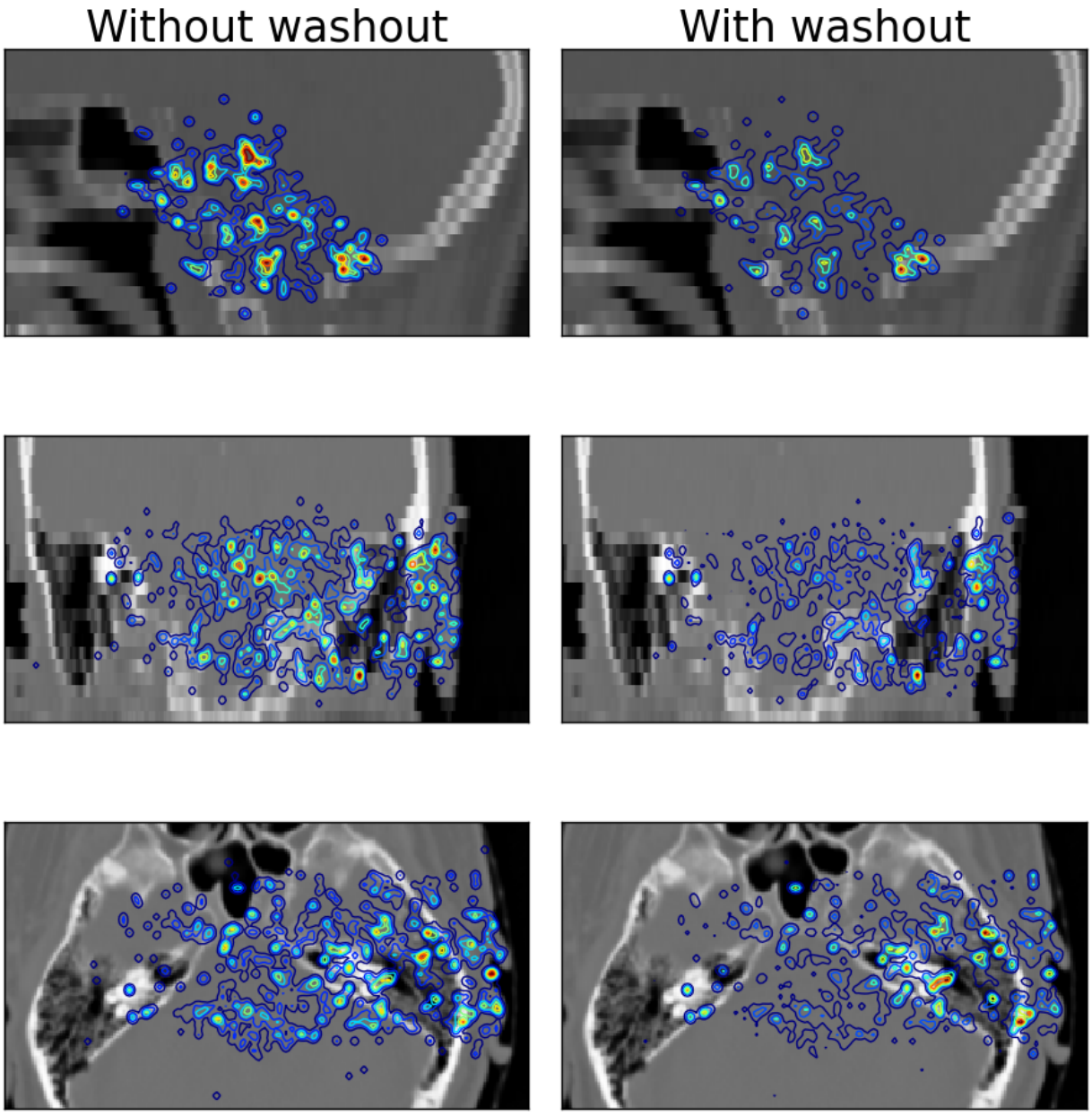


Figure 4.19: Annihilation photons following the decay of $^{13}N$ with and without Washout, time set from minute 10 to 40, radiotherapy plan, $10^7$ protons, patient head CT. Top: Without washout, Bottom: With washout

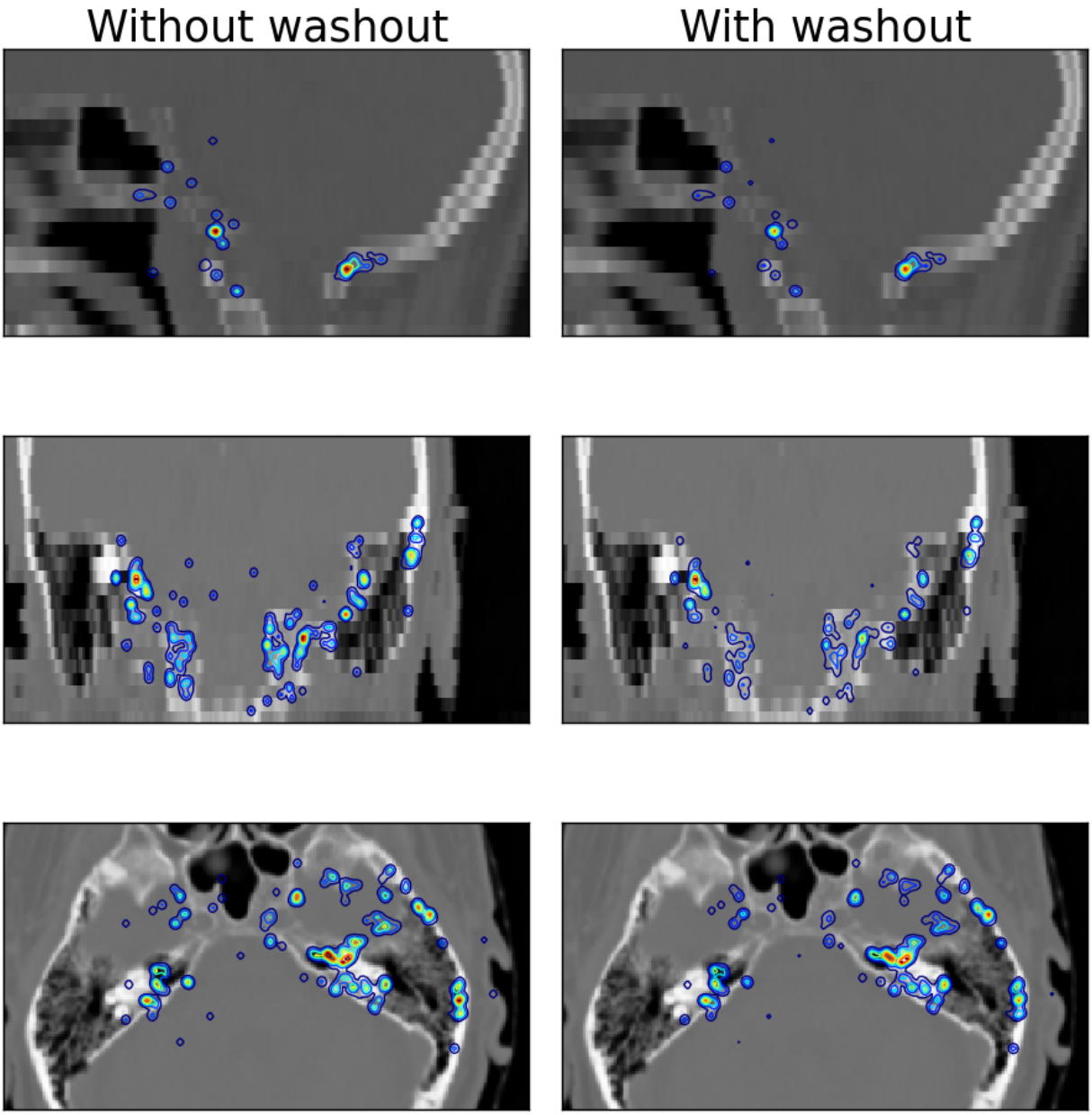


Figure 4.20: Annihilation photons following the decay of $^{38}$K with and without Washout, time set from minute 10 to 40, radiotherapy plan, $10^7$ protons, patient head CT. Top: Without washout, Bottom: With washout

As the washout effect is mainly due to blood flowing effects, it is not a surprise that there is almost no washout in the bone area. This effect can be clearly seen at the transverse plane of figure 4.18.
The reduction of $^{38}K$ is not as large, because it can be found mostly in the bones, areas with low blood flow.

Table 4.6 depicts the number of decayed $\beta^+$-emitters during offline PET monitoring. It was assumed that the monitoring takes place from minute 10 until minute 40. In total, the number of decays is 56% lower with washout than without considering the washout.

Table 4.6: Percentage of selected $\beta^+$-emitters decaying during offline PET monitoring with and without washout

| $\beta^+$-emitter | Percentage without washout | Percentage with washout |
|---|---|---|
| $^{11}C$ | 92.42% | 92.45% |
| $^{13}N$ | 5.87% | 5.54% |
| $^{15}O$ | 0.6% | 0.57% |
| $^{38}K$ | 1% | 1.36% |
| $^{30}P$ | 0.06% | 0.08% |

### 4.3.2 Depth-dependent distributions with washout

Figure 4.21 permits a closer investigation of the depth-dependent distribution of selected nuclides during PET monitoring (minute 10 to 40). We can see that the washout effect causes a significant reduction of the activity. $^{13}$N, $^{15}$O and $^{11}$C fall to less than a half of their activity without washout. Besides, a stronger decline on the left side (the soft tissue area) of these three curves, can be observed. This causes a tilt to the left in the case of $^{13}$N, and a more even distribution of $^{15}$O and $^{11}$C. Again, it can be seen that the washout of $^{38}$K is significantly lower than in other nuclides.
The curves were smoothed to reduce the spikes which still can be seen in the following figures. The spikes result from the different voxel sizes of CT and source file.

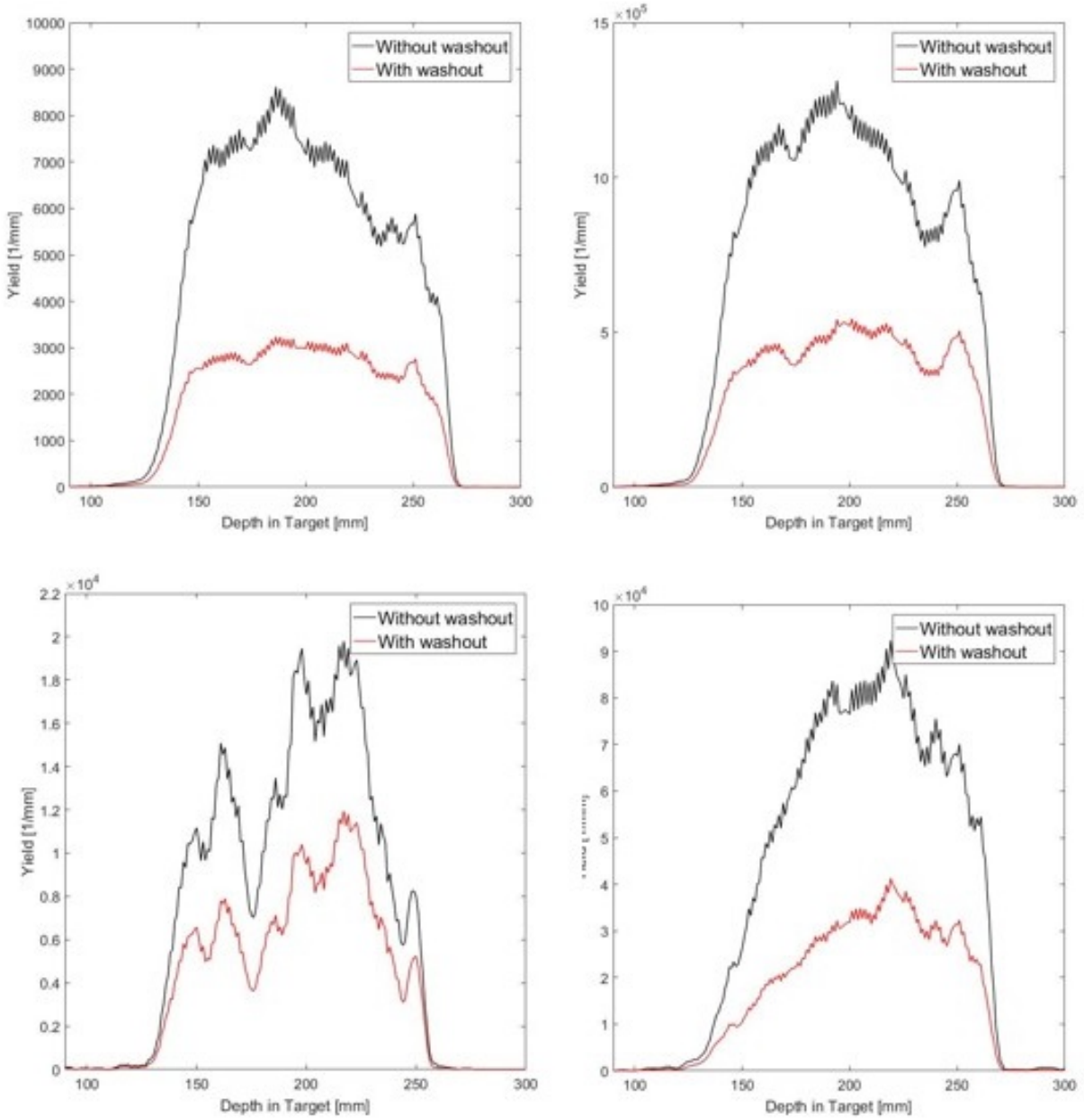


Figure 4.21: Depth-dependent 1D distribution with and without washout in direction of $x$, radiotherapy plan, $10^7$ protons, patient head CT, irradiation time set to 0, curves were smoothed. Top left: $^{15}$O, Top right: $^{11}$C, Bottom left: $^{38}$K, Bottom right: $^{13}$N

The comparison between figure 4.22 and 4.23 shows that the depth-dependent distribution changes due to the washout effect. It can be seen that the curves become significantly lower at the area with HU zero, hence tissue with high blood flow. Also, a minimal relative rise of $^{30}$P and $^{38}$K in comparison to the other nuclides can be detected after washout.
The beam enters the body from the right side of the graph. Shortly before the beam is stopped in the tissue, the curves fall to zero again. The time of acquisition was set from 10 to 40 minutes.

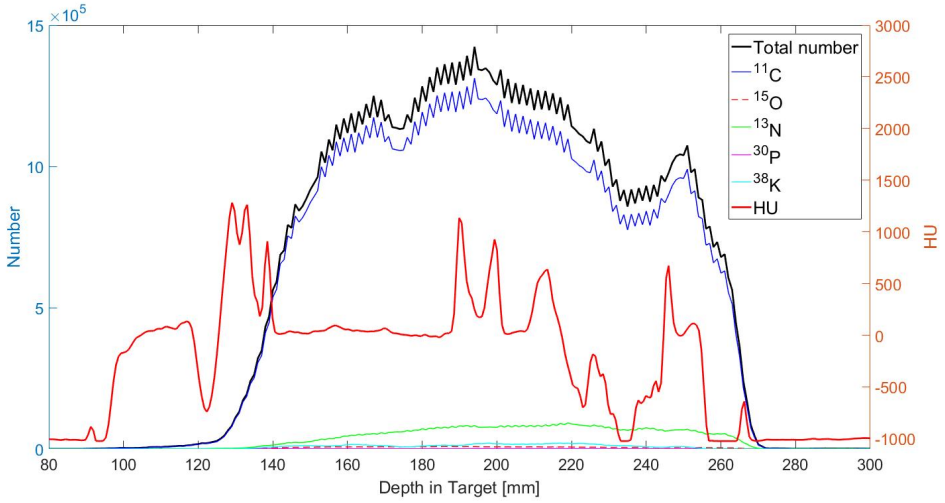


Figure 4.22: Depth-dependent distribution of annihilation photons without washout, radiotherapy plan, $10^7$ protons, patient head CT, curves were smoothed

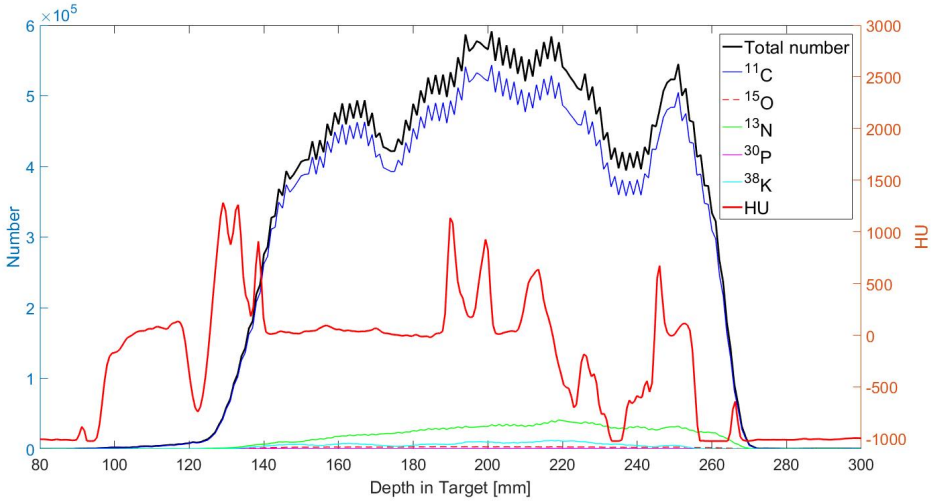


Figure 4.23: Depth-dependent distribution with washout, radiotherapy plan, $10^7$ protons, patient head CT, curves were smoothed

The depth-dependent distribution of $^{11}$C seems to be similar to the distribution of the overall yield. Figure 4.24 allows a more precise comparison between these two distributions. The curve of $^{11}$C was normalized, and multiplied with a factor to overlay with the overall yield. For the overall yield, only $^{11}$C, $^{15}$O, $^{13}$N, $^{30}$P and $^{38}$K were considered.
A few discrepancies can still be observed. However, particularly the distal edge of $^{11}$C matches precisely with the distal edge of the overall yield. Therefore, it can be assumed that the simulation of $^{11}$C is sufficient for range verification.

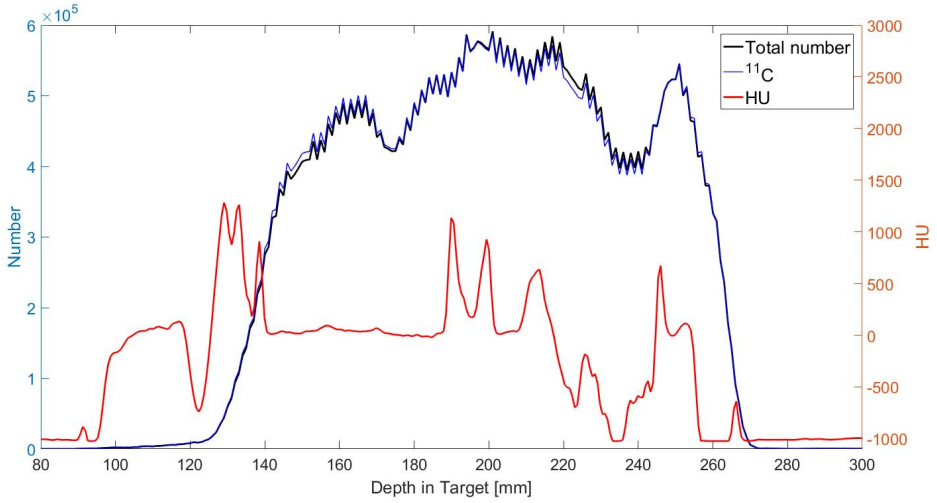


Figure 4.24: Depth-dependent distribution of $^{11}$C normalized to distribution of all nuclides, radiotherapy plan, $10^7$ protons, patient head CT, curves were smoothed

However, if a more accurate approximation of the depth-dependent distribution is needed, $^{13}$N should be included in the model. Figure 4.25 depicts the differences of the summed curve of $^{13}$N and $^{11}$C, and the curve of all nuclides. A slight improvement can be observed.
The point wise deviation drops from 1.3% in the case of just considering $^{11}$C, to 0.34% when considering $^{13}$N and $^{11}$C. Including additionally $^{15}$O, deteriorates the deviation slightly, it adds up to 0.36%. After including $^{38}$K, the point wise deviation drops to 0.07%.
For the point wise deviation, only the depths from 110 to 270 mm, hence 160 points, were considered, in order to rule out deviations in areas outside of the patients head.

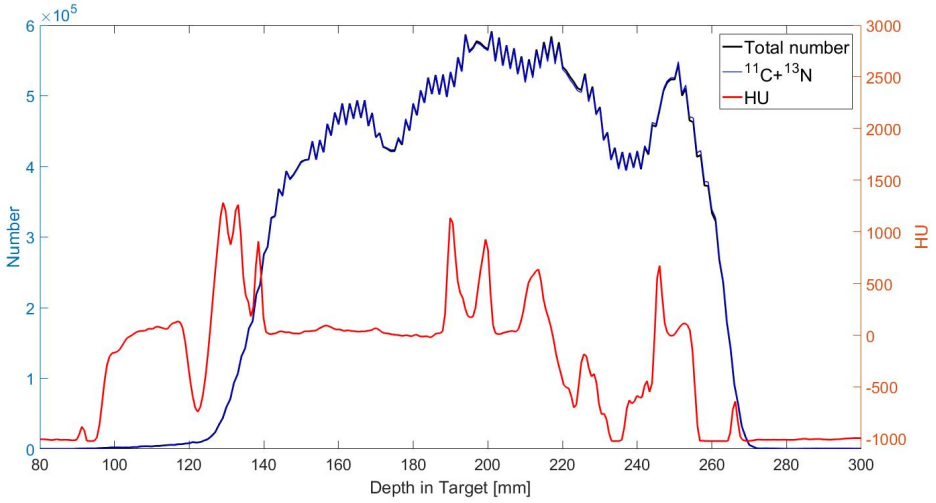


Figure 4.25: Depth-dependent distribution of $^{11}$C and $^{13}$N normalized to distribution of all nuclides, radiotherapy plan, $10^7$ protons, patient head CT, curves were smoothed

# 5 Summary and conclusion

One part of the present work was the evaluation of the CS-Actor and the PS-Actor in GATE. They were compared to experimental data to determine their accuracy. The irradiation of a PMMA box with beams of 140 and 175 MeV, providing both the yield of $^{11}C$ and $^{15}O$ was simulated. Furthermore, execution time of the CS-Actor was analysed. The other part of this work was the modelling of the $\beta^+$-activity after proton therapy. The yields of the produced nuclides were simulated by using a PMMA box, as well as a CT scan, as target, and a proton pencil beam, as well as a full therapy plan, as source. The influence of the incorporation of the irradiation time and biological washout was examined.

## 5.1 CS-Actor

Based on the comparison to the experimental data in section 4.1.1, it can be stated that both the CS-Actor and the PS-Actor underestimate the measured values. However, the CS-Actor corresponds much more accurately to the shape of the experimental curve. This is the case for all simulated scenarios.

Regarding the required proton quantities that are needed for an accurate simulation with the CS-Actor, $10^4$ seems to be enough, as the deviation to the values produced by $10^8$ protons (assumed as relatively accurate comparative values) is already under 1% (see table 4.2).

In the choice of the proton quantity, execution time constraints need to be taken into account.
In a clinical case, several energy layers and several spots are used for the irradiation of the patient. So, if we assume 20-30 energy layers, and approx. 500 spots where each of them is simulated with a quantity of $10^4$ protons, $10^8$ protons would have to be simulated for the whole therapy plan ($10^4 \cdot 20 \cdot 500 = 10^8$).
To ensure an acceptable performance in clinical cases, the simulation time of of the first simulation step, i.e. the production of the $\beta^+$-emitters (in our case $10^8$ protons) should not be more than 1 week. So, the number of protons must be chosen to fulfil this requirement. At MedAustron, a server with 44 kernels is available for the simulations. The execution time of $10^8$ protons is about 2400 hours (see table 4.4). This would be divided by 44 kernels, which equals about 54 hours, hence fulfilling the requirement.
Therefore, $10^4$ protons would be a reasonable decision for simulations with the CS-Actor.
An advantageous property of the CS-Actor is the fact that the execution time is the same, no matter whether only $^{11}C$, or $^{11}C$ and $^{15}O$ are simulated.

The CS-Actor is relatively new, and can still contain some bugs or uncertainties due to unknown cross-section data. In section 4.2 it was discovered that the CS-Actor produces incorrect results for beams in the direction of $x$.
In section 4.2.3 a discrepancy compared to the PS-Actor in the depth-dependent yield of $^{15}O$ can be seen.

All in all, the CS-Actor shows promising results, and seems to be an applicable and faster alternative to simulations that fully rely on MC methods. However, the code still has some initial difficulties, which should be examined and corrected in further investigation. Above all, it should allow the irradiation in all directions.

## 5.2 Modelling of $\beta^+$-activity after proton therapy

The executed simulations illustrate the importance of including irradiation time, physical decay and biological washout in simulations for offline PET. It was shown that the biological washout changes the depth-distribution of the nuclides, and reduces the number of detectable decays during monitoring by approximately half (see section 4.3.2). Neglecting the irradiation time can produce a distorted simulation that overestimates nuclides with short half-lives (see figure 4.7).

In summary, it can be stated that, based on their number of nuclides, their half-lives, depth-dependent distributions, and after taking into account biological washout, $^{11}$C and $^{13}$N are the most important nuclides for PET monitoring in offline PET.

The simulation of $^{11}$C might be sufficient for range verification when analysing the distal fall of edge. However, including $^{13}$N can achieve a higher accuracy in the depth-dependent distribution. As long as the CS-Actor is not available for simulations of $^{13}$N, including $^{13}$N would mean more required resources and execution time. Therefore, an extension of the CS-Actor is desirable.
Because of its very high activity in the first 10 minutes, $^{15}$O should be included in simulations for in-beam and in-room PET as well. For offline PET, it is irrelevant, as it adds up to only 0.57% of the overall activity during offline PET monitoring (see table 4.6).
Due to its very short half-life, $^{10}$C, which is mentioned in several papers concerning other PET monitoring modalities, is not considered relevant for offline PET. Only for in-beam PET it is relevant, because of its high activity during the irradiation.
Based on the performed simulation, $^{30}$P, $^{34}$Cl and $^{39}$Ca are considered irrelevant for all types of PET monitoring.

Concerning the software GATE, the inclusion of the irradiation time

and the precise implementation of the time differences when simulating several irradiation fields are missing features that would be helpful in clinical application. If the simulation of $^{13}$N is desired, the extension of the CS-Actor would be beneficial for execution time and accuracy. For the extension of the CS-Actor, it is necessary to find reliable cross-section data for the desired nuclide. However, after finding cross-section data, the extension itself can be done quickly and easily. If we assume the inclusion of $^{13}$N, additionally to the simulation of $^{11}$C, the execution time would change as follow:
If the CS-Actor is used for the first step (simulation of $\beta^+$-emitters), the execution time for this step would not change, because the execution time of the CS-Actor stays the same, regardless of the number of nuclides.
Using the PS-Actor would mean a longer execution time, because the PS-Actor needs more statistic; $10^4$ initial protons for the CS-Actor compared to $10^7$ for the PS-Actor. Including a second nuclide would double the execution time of the first step.
The reading out of the photons, the second step, has to be done with the PS-Actor, as the CS-Actor is not available for photons. However, this is not a problem, because the second step can be performed in additional 2 minutes (when using 44 kernels).
Concerning storage requirements, the inclusion of $^{13}$N would cause additional 7 GB of temporary MetaImage data, produced by the GATE macros. One output file has a size of 80 MB. 88 output files are created by the GATE macros, 44 for every simulation when using 44 kernels. Additionally, the merged MetaImages of this temporary MetaImage data and the split sources occupy 2 MB of storage.

In conclusion, simulations with GATE have proved its worth and potential to be integrated in the clinical routine to assure an accurate and effective treatment with proton therapy.
To minimize uncertainties in the simulation, further examination could be done in the evaluation of the washout model, as it is especially crucial for offline PET.

The establishment and extension of the CS-Actor would be another step towards a faster and accurate alternative to full-MC simulations.

# List of Figures

# List of Tables

# Bibliography


[1] Eurostat. Eurostat Pressemitteilung: Nach wie vor jeder vierte Todesfall in der EU durch Krebs verursacht. http://ec.europa.eu/eurostat/documents/2995521/7150001/3-03022016-BP-DE.pdf/51dd300e-c157-4299-be63-157286c92268. [updated on Feb 3rd 2016, accessed on March 10th 2017].

[2] H. Rohling. *Simulation studies for the in-vivo dose verification of particle therapy*. Bericht des HZDR, HZDR-062, TU Dresden, 2015.

[3] S. Jan, G. Santin, D. Strul, S. Staelens, K. Assié, D. Autret, S. Avner, R. Barbier, M. Bardiès, P. M. Bloomfield, D. Brasse, V. Breton, P. Bruyndonckx, I. Buvat, A. F. Chatziioannou, Y. Choi, Y. H. Chung, C. Comtat, D. Donnarieix, L. Ferrer, S. J. Glick, C. J. Groiselle, D. Guez, P.-F. Honore, S. Kerhoas-Cavata, A. S. Kirov, V. Kohli, M. Koole, M. Krieguer, D. J. van der Laan, F. Lamare, G. Largeron, C. Lartizien, D. Lazaro, M. C. Maas, L. Maigne, F. Mayet, F. Melot, C. Merheb, E. Pennacchio, J. Perez, U. Pietrzyk, F. R. Rannou, M. Rey, D. R. Schaart, C. R. Schmidtlein, L. Simon, T. Y. Song, J.-M. Vieira, D. Visvikis, R. Van de Walle, E. Wieërs, and C. Morel. GATE - Geant4 Application for Tomographic Emission: a simulation toolkit for PET and SPECT. *Phys. Med. Biol.*, 49(19):4543–4561, 2004.

[4] U. Amaldi and G. Kraft. Radiotherapy with beams of carbon ions. *Rep. Prog. Phys.*, 68(8):1861, 2005.

[5] D. J. Scanderbeg and D. J. Starkschall. Hendee's Radiation Therapy Physics. *Wiley-Blackwell*, pages 204–214, 2016.

[6] G. R. Fois. *Monte Carlo simulation studies for spatially franctionated radiaation therapy techniques*. PhD thesis, Universita degli studi di Cagliari, Cagliari, 2012.

[7] M. A. Nunes. Hadron Therapy Physics and Simulations. *Springer Science & Business Media*, pages 1–6, 2013.

[8] R. R. Wilson. Radiological Use of Fast Protons. *Radiology*, 47(5):487–491, 1946.

[9] W.H. Brag and R. Kleeman. On the alpha particles of radium, and their loss of range in passing through various atoms and molecules. *Philos Mag*, pages 318–340, 1905.

[10] Sumitomo Heavy Industries. http://www.shi.co.jp/quantum/eng/product/proton/img/SOBP.png. [updated in 2010, accessed on March 10th 2017].

[11] T. Bortfeld, H. Paganetti, and H. Kooy. Proton Beam Radiotherapy — The State of the Art. *Med. Phys.*, 32(6):2048–2049, 2005.

[12] Particle Therapy Co-Operative Group. Facilities in Operation. https://www.ptcog.ch/index.php/facilities-in-operation". [updated in March 2017, accessed on March 10th 2017].

[13] M. Benedikt, J. Gutleber, M. Palm, W. Pirkl, U. Dorda, and A. Fabich. Overview of the MedAustron design and technology choices. *Proceedings of IPAC'10*, pages 109–111, 2010.

[14] EBG MedAustron GmbH. Home | MedAustron. https://www.medaustron.at/. [updated in 2017, accessed on March 10th 2017].

[15] F. Moser. *Energy verification in ion beam therapy*. PhD thesis, TU Wien, 2012.

[16] X. Zhu and G. El Fakhri. Proton Therapy Verification with PET Imaging. *Theranostics*, 3(10):731–740, 2013.

[17] M. Bauser and L. Lehmann. Positronen-Emissions-Tomographie. *Chemie in unserer Zeit*, 46(2):80–99, 2012.

[18] S. Helmbrecht. *Partikeltherapie-PET – Optimierung der Datenverarbeitung für die klinische Anwendung*. Bericht des HZDR, HZDR-058, TU Dresden, 2015.

[19] J. Langner. Development of a Parallel Computing Optimized Head Movement Correction Method in Positron Emission Tomography. Master's thesis, University of Apllied Sciences, Dresden, 2003.

[20] Georgy Shakirin, Daniela Kunath, Kristin Laube, Wolfgang Enghardt, Henning Braess, Fine Fiedler, Marlen Priegnitz, Wolfgang Enghardt, and Katia Parodi. Implementation and workflow for PET monitoring of therapeutic ion irradiation: A comparison of in-beam, in-room, and off-line techniques. *Physics in Medicine and Biology*, 56(5):1281–1298, 2011.

[21] C. Ammar, K. Frey, J. Bauer, C. Melzig, S. Chiblak, M. Hildebrandt, D. Unholtz, C. Kurz, S. Brons, J. Debus, A. Abdollahi, and K. Parodi. Comparing the biological washout of beta$^+$-activity induced in mice brain after 12c-ion and proton irradiation. *Phys. Med. Biol.*, 59(23):7229–7244, 2014.

[22] H. Rohling, L. Sihver, M. Priegnitz, W. Enghardt, and F. Fiedler. Comparison of PHITS, GEANT4, and HIBRAC simulations of depth-dependent yields of beta$^+$ -emitting nuclei during therapeutic particle irradiation to measured data. *Phys. Med. Biol.*, 58(18):6355–6368, 2013.

[23] K. Parodi, W. Enghardt, and T. Haberer. In-beam PET measurements of beta$^+$ radioactivity induced by proton beams. *Phys. Med. Biol.*, 47(1):21, 2002.

[24] J. Bauer, D. Unholtz, C. Kurz, and K. Parodi. An experimental approach to improve the Monte Carlo modelling of offline

PET/CT-imaging of positron emitters induced by scanned proton beams. *Phys. Med. Biol.*, 58(15):5193, 2013.

[25] K. Parodi, H. Paganetti, H. A. Shih, S. Michaud, J. S. Loeffler, T. F. Delaney, N. J. Liebsch, J. E. Munzenrider, A. J. Fischman, A. Knopf, and T. Bortfeld. Patient study of in vivo verification of beam delivery and range, using positron emission tomography and computed tomography imaging after proton therapy. *Int J Radiat Oncol Biol Phys*, 68(3):920–934, 2007.

[26] E. Seravalli, C. Robert, J. Bauer, F. Stichelbaut, C. Kurz, J. Smeets, C. Van Ngoc Ty, D. R. Schaart, I. Buvat, K Parodi, and F. Verhaegen. Monte Carlo calculations of positron emitter yields in proton radiotherapy. *Physics in Medicine and Biology*, 57(6):1659, 2012.

[27] I. Pshenichnov, I. Mishustin, and W. Greiner. Distributions of positron-emitting nuclei in proton and carbon-ion therapy studied with GEANT4. *Phys. Med. Biol.*, 51(23):6099–6112, 2006.

[28] S. Jan, T. Frisson, and D. Sarrut. GATE simulation of 12 C hadrontherapy treatment combined with a PET imaging system for dose monitoring: A feasibility study. *IEEE Transactions on Nuclear Science*, 60(1):423–429, 2013.

[29] J. Bauer, D. Unholtz, F. Sommerer, C. Kurz, T. Haberer, K. Herfarth, T. Welzel, S. E. Combs, J. Debus, and K. Parodi. Implementation and initial clinical experience of offline PET/CT-based verification of scanned carbon ion treatment. *Radiotherapy and Oncology*, 107(2):218–226, 2013.

[30] H. Mizuno, T. Tomitani, M. Kanazawa, A. Kitagawa, J. Pawelke, Y. Iseki, E. Urakabe, M. Suda, A. Kawano, R. Iritani, S. Matsushita, T. Inaniwa, T. Nishio, S. Furukawa, K. Ando, Y. K. Nakamura, T. Kanai, and K. Ishii. Washout measurement of radioisotope

implanted by radioactive beams in the rabbit. *Phys. Med. Biol.*, 48(15):2269–2281, 2003.

[31] L. L. Carter and E. D. Cashwell. Particle-Transport Simulation with the Monte Carlo Method. Technical Report TID–26607, Los Alamos Scientific Lab., N.Mex. (USA), January 1975.

[32] H. L. Anderson. Metropolis, Monte Carlo, And the Maniac. *Los Alamos Science*, 14:96–108, 1986.

[33] G. L. Trigg. Mathematical Tools for Physicists. *John Wiley & Sons*, pages 250–252, 2006.

[34] L. Sihver, T. Sato, M. Puchalska, and G. Reitz. Simulations of the MATROSHKA experiment at the international space station using PHITS. *Radiation and Environmental Biophysics*, 49(3):351–357, 2010.

[35] A. Ferrari, P. R. Sala, A. Fasso, and J. Ranft. FLUKA: A multi-particle transport code (Program version 2005). 2005.

[36] A. C. Kraan. Range Verification Methods in Particle Therapy: Underlying Physics and Monte Carlo Modeling. *Frontiers in Oncology*, 5, 2015.

[37] L. Sihver, D. Schardt, and T. Kanai. Depth-Dose Distributions of High-Energy Carbon, Oxygen and Neon Beams in Water. *Japanese Journal of Medical Physics*, 18(1):1–21, 1998.

[38] L. Sihver and D. Mancusi. Present status and validation of HIBRAC. *Radiation Measurements*, 44(1):38–46, 2009.

[39] S. Agostinelli, J. Allison, K. Amako, J. Apostolakis, H. Araujo, P. Arce, M. Asai, D. Axen, S. Banerjee, G. Barrand, F. Behner, L. Bellagamba, J. Boudreau, L. Broglia, A. Brunengo, H. Burkhardt, S. Chauvie, J. Chuma, R. Chytracek, G. Cooperman,

G. Cosmo, P. Degtyarenko, A. Dell'Acqua, G. Depaola, D. Dietrich, R. Enami, A. Feliciello, C. Ferguson, H. Fesefeldt, G. Folger, F. Foppiano, A. Forti, S. Garelli, S. Giani, R. Giannitrapani, D. Gibin, J. J. Gomez Cadenas, I. Gonzalez, G. Gracia Abril, L. G. Greeniaus, W. Greiner, V. Grichine, A. Grossheim, P. Gumplinger, R. Hamatsu, K. Hashimoto, H. Hasui, A. Heikkinen, A. Howard, V. Ivanchenko, A. Johnson, F. W. Jones, J. Kallenbach, N. Kanaya, M. Kawabata, Y. Kawabata, M. Kawaguti, S. Kelner, P. Kent, T. Kodama, R. Kokoulin, M. Kossov, H. Kurashige, E. Lamanna, T. Lampen, V. Lara, V. Lefebure, F. Lei, M. Liendl, W. Lockman, F. Longo, S. Magni, M. Maire, E. Medernach, K. Minamimoto, P. Mora de Freitas, Y. Morita, K. Murakami, M. Nagamatu, R. Nartallo, P. Nieminen, T. Nishimura, K. Ohtsubo, M. Okamura, S. O'Neale, Y. Oohata, K. Paech, J. Perl, A. Pfeiffer, M. G. Pia, F. Ranjard, A. Rybin, S. Sadilov, E.f Di Salvo, G. Santin, T. Sasaki, N. Savvas, Y. Sawada, S. Scherer, S. Sei, V. Sirotenko, D. Smith, N. Starkov, Horst Stoecker, J. Sulkimo, M. Takahata, S. Tanaka, E. Tcherniaev, F. Safai Tehrani, M. Tropeano, P. Truscott, H. Uno, L. Urban, P. Urban, M. Verderi, A. Walkden, W. Wander, H. Weber, J. P. Wellisch, T. Wenaus, D. C. Williams, D. Wright, T. Yamada, H. Yoshida, and D. Zschiesche. GEANT4: A Simulation toolkit. *Nucl.Instrum.Meth.*, A506:250–303, 2003.

[40] OpenGATE collaboration. GATE - Simulations of Preclinical and Clinical Scans in Emission Tomography, Transmission Tomography and Radiation Therapy. http://www.opengatecollaboration.org/. [updated n.d., accessed on March 10th 2017].

[41] OpenGATE collaboration. Users Guide V7.2 - Wiki OpenGATE. http://wiki.opengatecollaboration.org/index.php/Users_Guide_V7.2. [updated on June 21st 2016, accessed on March 10th 2017].

[42] I. Martínez-Rovira, C. Jouvie, and S. Jan. Technical note: Implementation of biological washout processes within

GATE/GEANT4–a Monte Carlo study in the case of carbon therapy treatments. *Med. Phys.*, 42(4):1773–1778, 2015.

[43] U. Harten. Physik: Einführung für Ingenieure und Naturwissenschaftler. *Springer-Verlag Berlin Heidelberg*, pages 363–364, 2005.

[44] Technical University Dresden. Reactor training course: Experiment "Activation and decay of radioactive nuclides", 2015.

[45] National Institute of Standards and Technology. Stopping-power and range tables for protons-PSTAR-Physical Measurement Laboratory. http://physics.nist.gov/PhysRefData/Star/Text/PSTAR.html. [updated on Nov. 23rd 2016, accessed on March 10th 2017].

# 6 Appendix

## 6.1 Comparison PS-Actor and CS-Actor

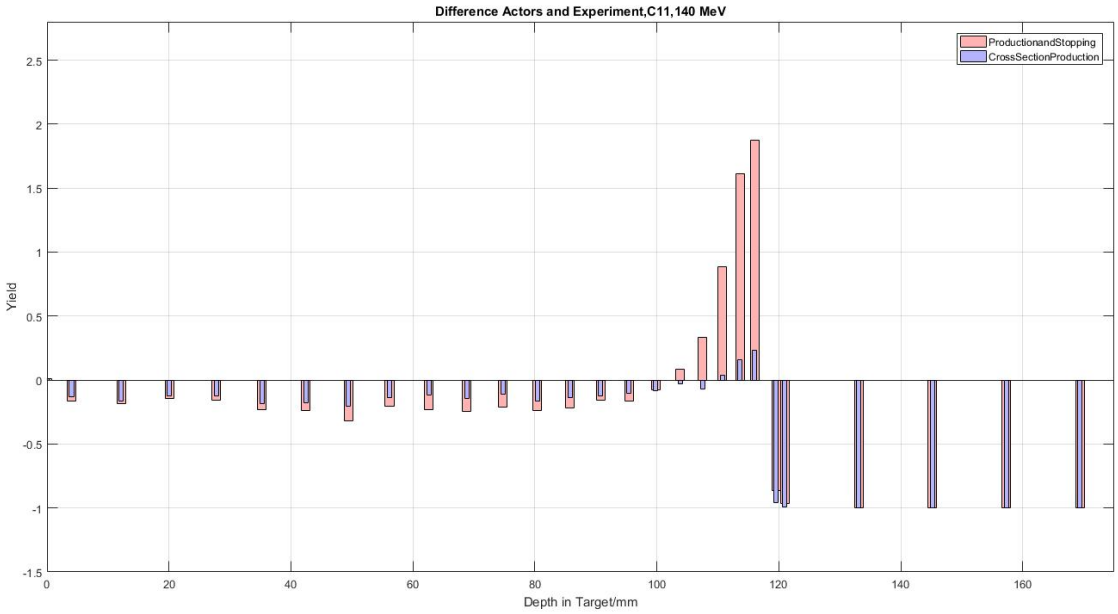


Figure 6.1: Differences between CS-Actor, PS-Actor and experimental data for $^{11}C$, resulting from proton irradiation (140 MeV, $10^7$ protons) of a PMMA target

## 6.2 Depth-dependent amounts of $\beta^+$-emitters

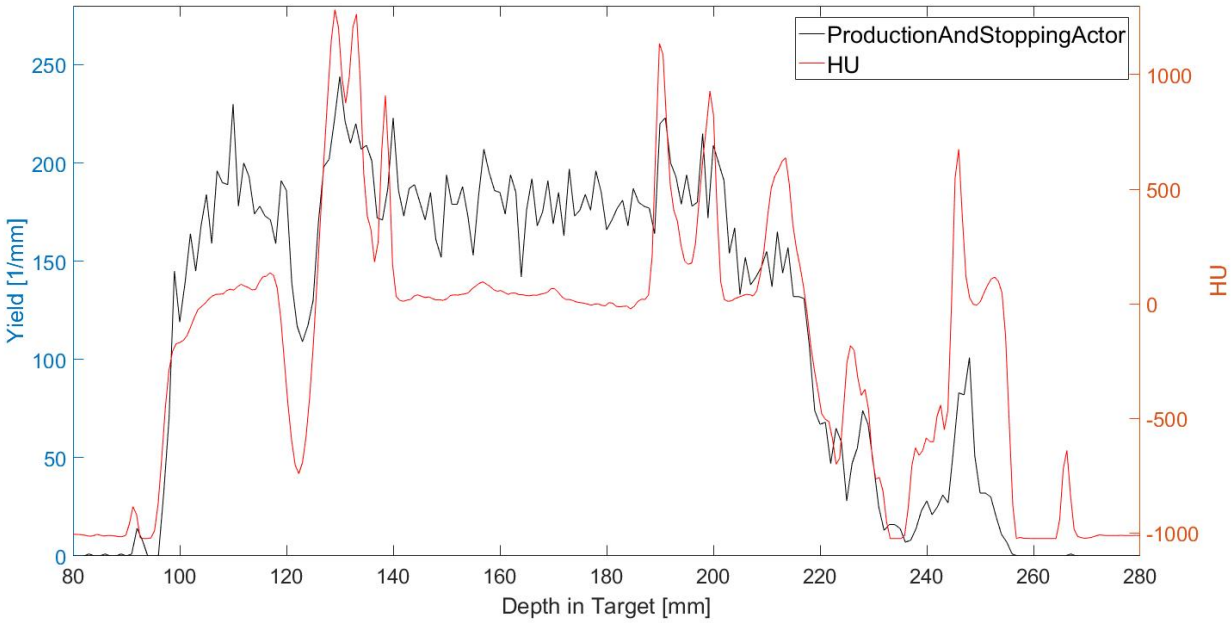


Figure 6.2: Depth-dependent distribution of $^{10}$C, 150 MeV, proton beam, $10^7$ protons, patient head CT

## 6.3 Depth-dependent distributions with washout

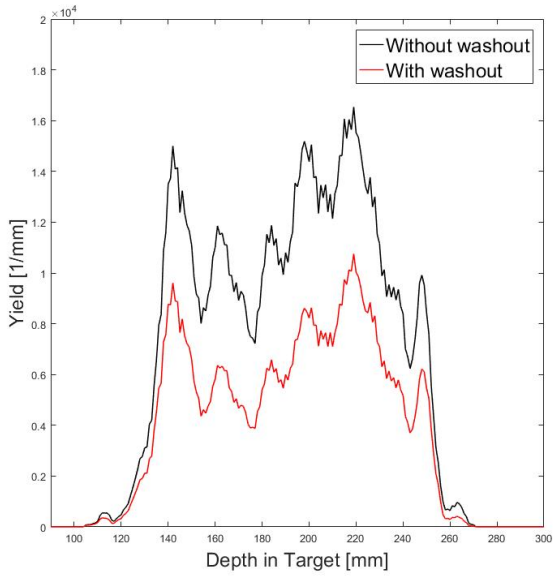


Figure 6.3: Depth-dependant 1D-profile of $^{30}$P with and without washout, radiotherapy plan, $10^7$ protons, patient head CT

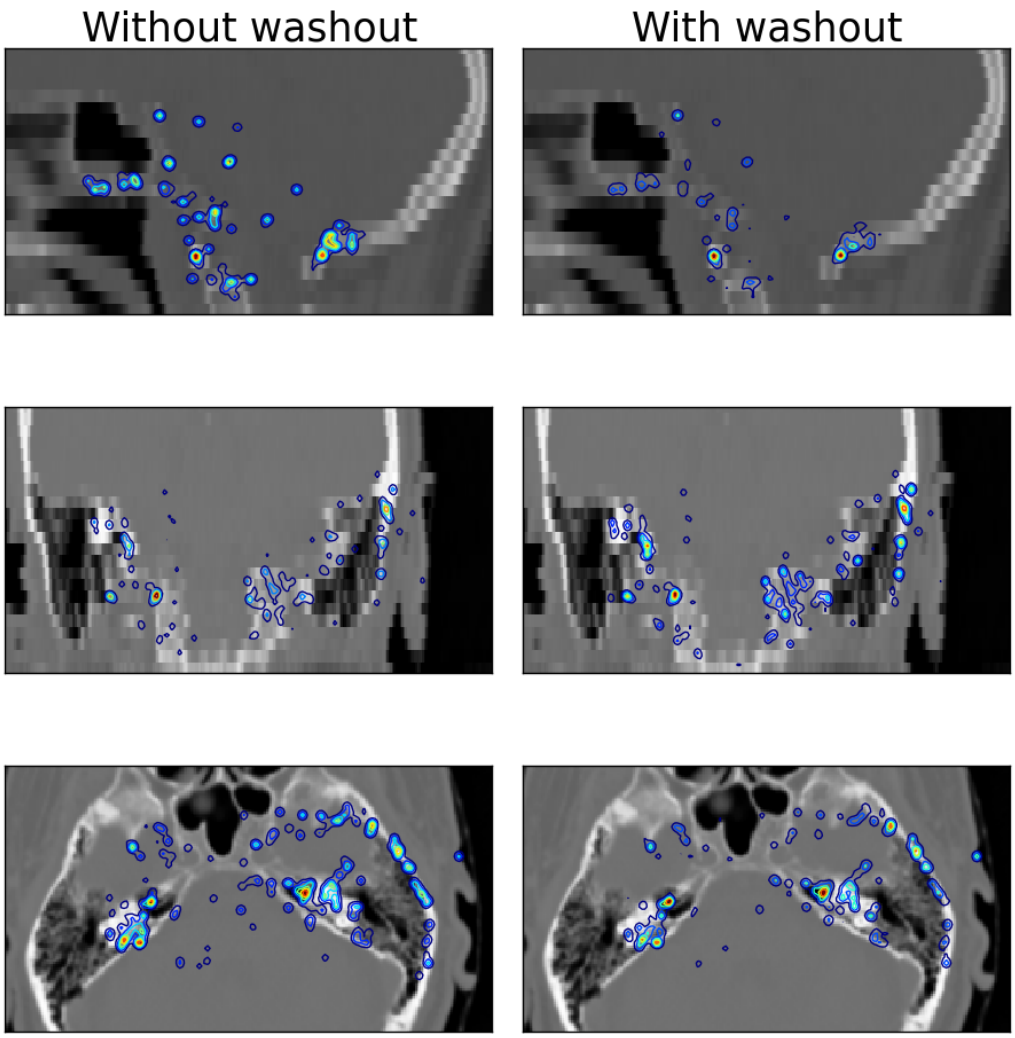


Figure 6.4: Annihilation photons following the decay of $^{30}$P with and without Washout, radiotherapy plan, $10^7$ protons, patient head CT. Top: Without washout, Bottom: With washout

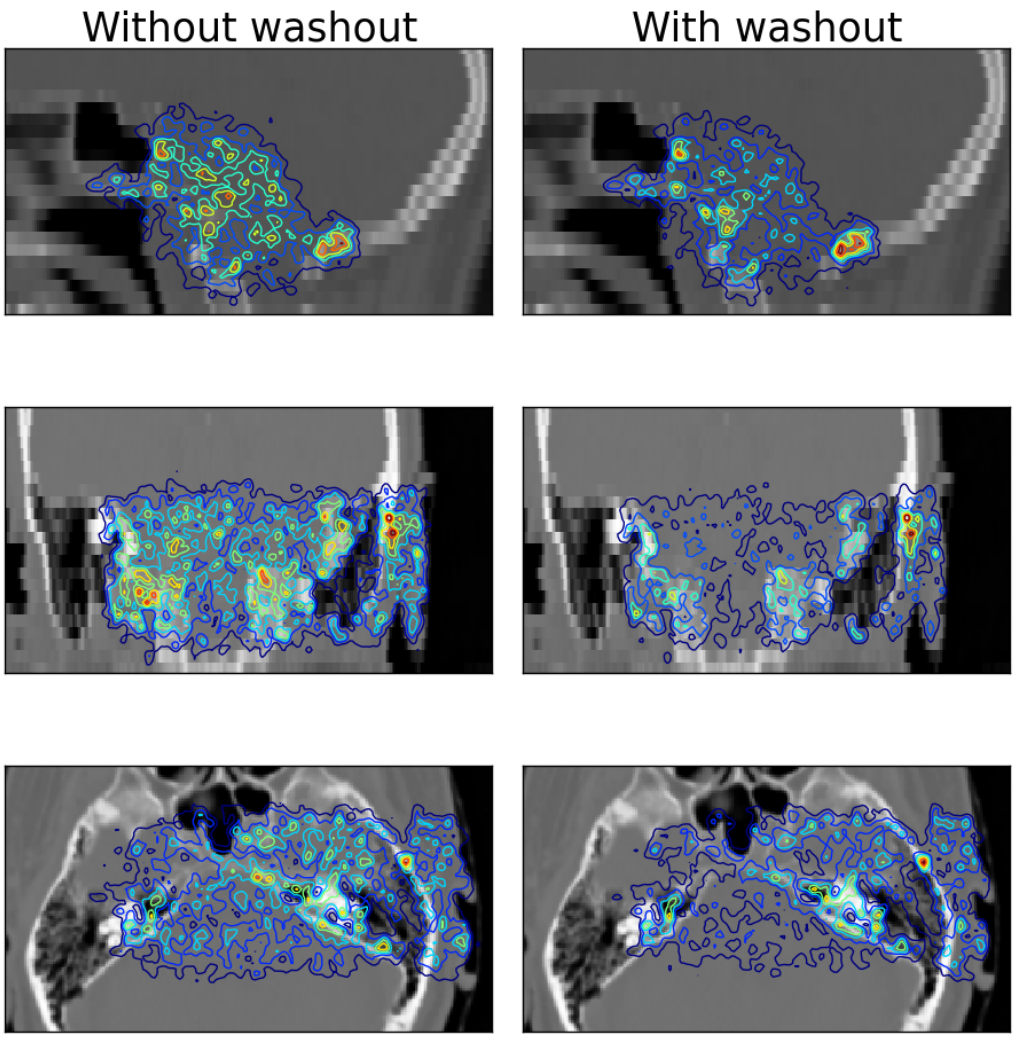


Figure 6.5: Annihilation photons following the decay of $^{11}C$ with and without Washout, radiotherapy plan, $10^7$ protons, patient head CT. Top: Without washout, Bottom: With washout

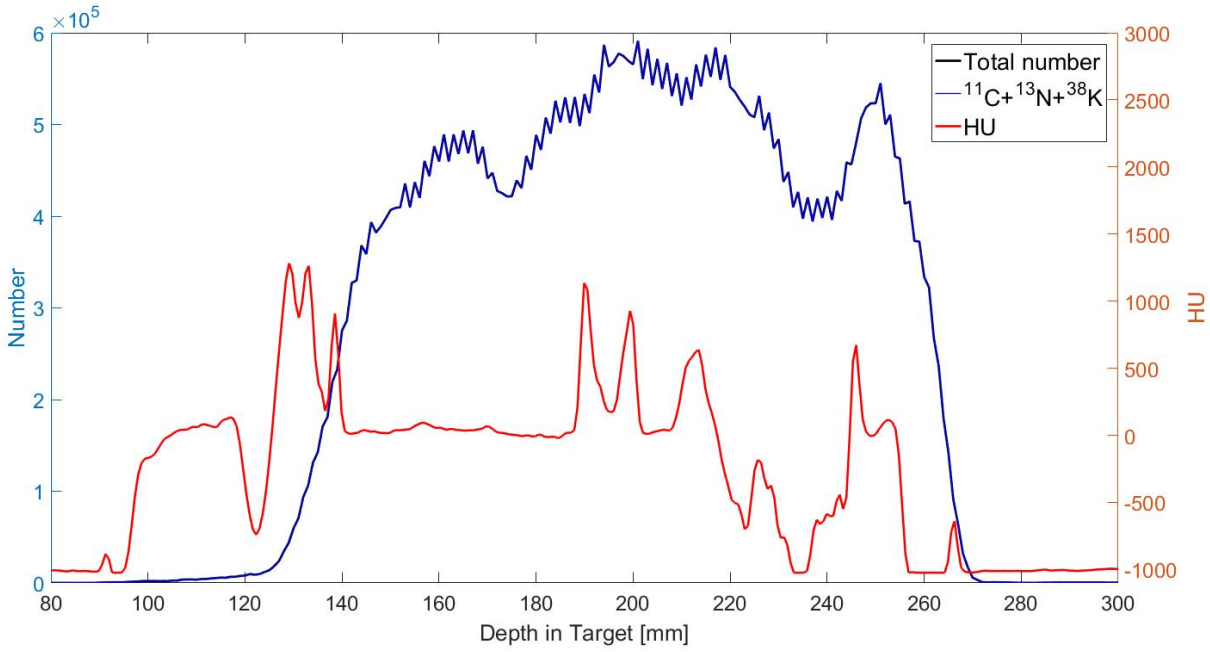


Figure 6.6: Depth-dependent distribution of $^{11}$C, $^{38}$K and $^{13}$N normalized to distribution of all nuclides, radiotherapy plan, $10^7$ protons, patient head CT